

The oscillatory pipe flow with arbitrary wall injection

BY JOSEPH MAJDALANI¹ AND GARY A. FLANDRO²

¹*Department of Mechanical and Industrial Engineering,
Marquette University, Milwaukee, WI 53233, USA*

²*Advanced Space Propulsion Center, University of Tennessee Space Institute,
Tullahoma, TN 37388, USA*

*Received 26 April 2001; revised 30 August 2001; accepted 2 October 2001;
published online 20 May 2002*

The linearized Navier–Stokes equations play a central role in describing the unsteady motion of a viscous fluid inside a porous tube. Asymptotic solutions of these equations have been found and here we extend the class of known solutions by solving the problem for an arbitrary mean-flow function of the Berman type. In the process, we show how not only do we recover, confirm, or correct some of the previously known solutions, but also find some completely new forms. It is interesting that, for sufficiently small injection, the Sexl profile can be restored from ours. Furthermore, we find that analytical, numerical and experimental results obtained by other investigators compare favourably with ours. The methods we apply provide accurate expressions for the main flow variables and help describe the ensuing oscillatory field. By appealing to a space-reductive multiple-scale technique, the problem's underlying length-scale is rigorously derived. Our results indicate that, irrespective of the mean-flow details, the unsteady component of vorticity initiated by small pressure disturbances can be more intense than its mean counterpart. No vortical study in porous tubes can therefore be complete unless it incorporates the unsteady field contribution.

Keywords: Stokes flow; periodic flow; porous wall; perturbation theory; WKB; multiple scales

1. Introduction

Much attention has been given to the description of internal flows established inside circular tubes with porous walls. Depending on whether fluid is being added or withdrawn, examples cited in the literature have ranged from paper making (Taylor 1956), to the modelling of biological flows (Goto & Uchida 1990), to simulations of the combustion-induced gas motion inside solid rocket motors (Culick 1966). Research was spurred on by a series of interesting technological processes. Pertinent applications have included flow filtration, isotope separation, surface ablation, pulmonary circulation, and arterial blood flow modelling. Whereas earlier studies have focused on steady laminar flow analyses, the more challenging temporal aspects have been deferred to later investigations. In order to gain perspective on the problem at hand, a brief summary will now be presented.

The earliest account of steady flow solutions in channels with porous boundaries can be attributed to Berman (1953). Provided that fluid was being injected or removed uniformly through the sidewalls, Berman was able to introduce a technique that reduced the Navier–Stokes system into a single ordinary differential equation. Following Berman’s landmark paper, a number of studies appeared in succession. Most were often valid over restricted ranges of fluid injection or suction. Further studies addressed the issue of spatial development and stability along with the existence of unique or multiple solutions. Experimental investigations were reported as well.

For circular pipes and tubes, Yuan & Finkelstein (1956) presented asymptotic solutions in the limiting cases of small suction and both small and large injection. Their formulation depended on the crossflow Reynolds number R . This key parameter was based on the uniform injection speed V , tube radius a , and kinematic viscosity ν . For large R , their solution correctly reduced to the inviscid expression reported by Taylor (1956), that same year, for infinite injection.

After classifying each type of possible solutions based on the ranges of R , Terrill & Thomas (1969) attempted the method of inner and outer expansions to derive asymptotic solutions for each separate class. Contrary to the existing formulations of Yuan & Finkelstein (1956), their approach indicated possible multiplicity of solutions. It captured the viscous layer at the pipe centre and predicted two solutions for fixed injection rate. In later studies, Durlafsky & Brady (1984) would demonstrate the illegitimacy of one of their two solutions.

Since Terrill & Thomas (1969) could not distinguish between the two apparent types for the large suction case, Terrill (1973) invested further exploratory effort. He was able to show that inclusion of exponentially small terms in the method of asymptotic expansions could produce more accurate results. These corrective terms could serve to predict the range of values for which no solutions could be found numerically. A formal asymptotic analysis led by Skalak & Wang (1978) concurred with Terrill’s predictions. Thus it was concluded that there existed at least two solutions for injection and, at most, four solutions for sufficiently large suction. In the process, elegant arguments were given regarding the necessary presence of multiple solutions for a given R . This issue was laid to rest following a rigorous mathematical treatment by Lu (1994). In summary, it was found that two solutions for injection, one being unphysical, existed for all R . For suction, two solutions existed in the ranges $[0, 2.3]$ and $[9.1, 20.6]$, no solution existed in $[2.3, 9.1]$, and four solutions were possible when the suction Reynolds number exceeded 20.6. In this article, the only physical solution for injection will be of concern.

Using Berman’s similarity transformation in a different physical setting, Brady & Acrivos (1981) employed matched asymptotic expansions to treat the general problem of a tube with a linearly accelerating surface velocity. Inasmuch as the porous pipe flow problem could be reproduced from their generalized formulation, their results shared similar features to the foregoing predictions. The spatial stability of such self-similar flows was later addressed by Durlafsky & Brady (1984). The physicality of corresponding similarity solutions was examined via small perturbations in the streamwise velocity. Taking into account the finite pipe length and the poor likelihood of an inlet velocity satisfying the similarity requirements, Brady (1984) studied the spatial development of the velocity structure for arbitrary inlet profiles with suction or injection. He found that, when a critical suction Reynolds number was reached, the influence of inlet conditions extended throughout the tube. This

behaviour prevented the similarity solution from evolving and caused, instead, collision regions to form near the head end. No such patterns were found with injection.

The influence of both symmetric and asymmetric perturbations was investigated numerically, for the injection case, by Gol'dshtik & Ersh (1989). Details showed that laminar solutions representing straight-through flow were stable for all injection. Conversely, solutions containing an axial reverse-current zone were absolutely unstable, indicating the non-physicality of such solutions. For injection Reynolds numbers exceeding 100, their numerical solution agreed with the asymptotic formulation of Yuan & Finkelstein (1956).

Other flow properties, such as skin friction and heat transfer coefficients, have also been examined. The onset of turbulence is another issue that several investigators have attempted to characterize. For steady conditions, useful data can be gathered from Wageman & Guevara (1960), Yuan & Brogren (1961), Olson & Eckert (1966), Sviridenkov & Yagodkin (1976), Beddini (1986) and Dunlap *et al.* (1990). The foregoing studies have confirmed the existence of a laminar segment whose size depended on the crossflow Reynolds number. They have also indicated that mean turbulent profiles differed only slightly from their laminar counterparts derived, for example, by Yuan & Finkelstein (1956). Such studies reinforced the importance of laminar solutions.

The challenges of modelling flows inside porous tubes rises to a new level of complexity when oscillatory wave motion is superimposed. Such has been the case when cold-flow simulations were undertaken for the purpose of understanding the internal gas dynamics during solid propellant burning. A number of experimental studies have, in fact, attempted to capture the nature of velocity oscillations inside tubes with transpiring walls. Tests realized on reactive propellants have spanned a range of almost four decades. In order to both reduce the hazards of dealing with live propellants and facilitate data acquisition, alternative procedures were sought at times. The goal was to relay the inherent fluid dynamics while relying on safe simulations of the gas addition process. The answer was found, partly, in pursuing cold-flow simulations of the injection mechanism.

Several investigators have undertaken cold-flow experiments that use nitrogen, carbon dioxide, or air to simulate the injectant (see, for example, Dunlap *et al.* 1990; Ma *et al.* 1990, 1991; Barron *et al.* 2000; Griffond & Casalis 2001; Casalis *et al.* 1998). Most of these studies concentrated on reproducing an acoustic setting of the closed–closed boundary type. Such a setting pertained to chambers that comprised impermeable head-end walls and choked flow at the downstream end. Acoustic closure at the aft end simulated rocket motors that (invariably) ended with a choked De Laval nozzle. Imposition of acoustic conditions of the closed–open type were also considered in cold-flow studies of nozzleless tubes. Being reserved to fewer applications, acoustic environments of the closed–open type received less attention. In the current study, formulations that apply to both acoustic types will be made available. However, the physical description will focus on the closed–closed configuration.

Mathematical modelling of the oscillatory field over transpiring surfaces was chiefly developed by Culick (1966) and Flandro (1974, 1989, 1995*a, b*). In fact, the first analytical solution for the oscillatory field with infinitely large injection was successfully derived by Flandro (1989). This formulation was fictitiously two dimensional: it ignored the downstream convection of unsteady vorticity and the radial depreciation of Taylor's mean-flow profile. Consequently, it only applied to a small region above the porous wall and a restricted range of physical parameters. An asymptotic

solution by Majdalani & Van Moorhem (1995, 1997) followed. The latter employed the exact Taylor profile yet shared its precursor's inability to incorporate the axial dependency.

An inviscid solution that incorporated the correct Taylor profile and axial dependency was later presented by Flandro (1995*a*). This was quickly followed by an improved asymptotic solution that included viscous effects (Flandro 1995*b*). A practically equivalent solution was derived by Majdalani & Van Moorhem (1995) using multiple-scale expansions. As shown by Majdalani & Van Moorhem (1998), both multidimensional solutions concurred with numerical simulations. They also showed fair agreement with data gathered from cold-flow experiments by Brown *et al.* (1986) and Dunlap *et al.* (1990). Later, the multiple-scale solution was used to disclose the character of the Stokes boundary-layer structure in porous tubes (Majdalani 1999). Recently, the analogous problem arising in a planar channel has been addressed by Majdalani & Roh (2000).

Following Flandro's work, Zhao *et al.* (2000) resorted to multiple scales in order to analyse the developing transient flow that preceded the inception of steady-state oscillations. Zhao's approach provided a crude approximation since it was based on a conjectured set of scales found by intuition. Being the product of guesswork, these scales were different from the uniformly valid scales that were prescribed by the problem's solvability condition. As such, they differed from those derived by Majdalani (1998) and Majdalani & Roh (2000).

It should be pointed out that most existing analytical solutions for the oscillatory field have been constructed by perturbing an initially steady mainstream that corresponds to the Taylor profile. As a result, they apply, in practice, to a very large influx through the peripheral walls. Such idealizations are quite suitable in simulating the relatively high rates of gas expulsion from propellant surfaces during solid rocket motor burning. In principle, they are limited to an infinitely large crossflow Reynolds number. On that account, it is the purpose of this article to generalize the techniques presented by Flandro (1995*a, b*) and Majdalani & Van Moorhem (1998) by extending their applicability to arbitrary levels of injection. The resulting solutions should be useful over a broader range of physical applications. The article also serves as a vital extension to the planar solution presented recently by Majdalani & Roh (2000). Another novelty is that, whereas a partial Wentzel–Kramers–Brillouin (WKB) solution was presented before, a rigorous asymptotic treatment will be offered in § 4 leading to a complete WKB solution. In particular, the characteristic length-scales that arise in the circular tube will now be derived using two space-reductive techniques in §§ 5 and 6. While one appeals to Prandtl's principle of matching by supplementary expansions, the other will apply the principle of least singular behaviour. For confirmation purposes, multiple independent verifications will be presented starting in § 7 with comparisons to other solutions. This is followed by a discussion in § 8, wherein experimental and numerical verifications are provided based on the work carried out by Brown *et al.* (1986) and Roh *et al.* (1995).

2. Problem formulation

(a) *The finite circular tube*

We consider the steady flow of a perfect gas in the region bounded by the porous walls of a cylindrical tube of radius a and finite length $L \gg a$. We assume that the

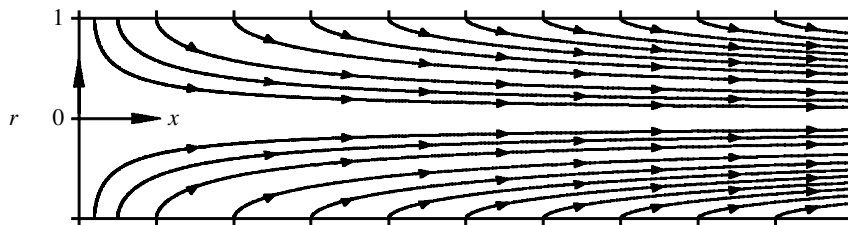


Figure 1. Axisymmetric system geometry including mean-flow streamlines.

speed of the gas at the wall V is uniform. We normalize the spatial variables by a and select a curvilinear coordinate system whose origin is anchored at the tube’s head-end centre. As shown in figure 1, x and r can be used to denote the non-dimensional streamwise and radial coordinates. Axial symmetry reduces the field investigation to the domains $0 \leq x \leq l$ and $0 \leq r \leq 1$, where $l = L/a < 70$. The tube is closed at $x = 0$ corresponding to a zero inlet profile in Berman’s formulation. As a result of this, the mainstream described by the streamline patterns of figure 1 is completely induced by the injection process. Inasmuch as we consider the case of choked flow at $x = l$ (where a nozzle can be located), we provide formulations that apply to an isobaric opening as well. The oscillatory field that we wish to evaluate will exist when the undisturbed state is perturbed via sinusoidal pressure oscillations of frequency ω and amplitude A . If c is the speed of sound, we follow Majdalani & Roh (2000) by limiting our scope to low crossflow Mach numbers ($M = V/c < 0.01$) and small A by comparison with the mean stagnation pressure p_s .

(b) Arbitrary mean-flow profile

Our point of departure is the self-similar mean-flow solution in a tube with porous walls. Following Berman (1953) or Yuan & Finkelstein (1956), we select a steady stream function Ψ that varies linearly in x . Without compromising generality, we employ $\Psi(x, r) = xF(r)$ (cf. Weissberg 1959; Brady & Acrivos 1981) and collapse the Navier–Stokes equations into

$$r^3 F'''' + r^2 R F''' (F - 2\varepsilon) + R(F' - r F'') [r F' + 3(F - \varepsilon)] = 0, \quad \varepsilon \equiv 1/R. \tag{2.1}$$

In our notation, $R = Va/\nu > 0$ for injection. The mainstream velocity and vorticity vectors (normalized by V) can be expressed as $\mathbf{u}_0 = u_0 \mathbf{e}_x + v_0 \mathbf{e}_r$ and $\boldsymbol{\Omega}_0 = \Omega_0 \mathbf{e}_\theta$. Boundary conditions include the no-slip, $u_0(x, 1) = 0$, radial influx at the wall, $v_0(x, 1) = -1$, axial symmetry, $\partial u_0(x, 0)/\partial r = 0$, and boundedness, $v_0(x, 0) = 0$. From the stream function definition, one can write

$$u_0 = \frac{x F'}{r}, \quad v_0 = -\frac{F}{r}, \quad \Omega_0 = \frac{x(F'/r - F'')}{r}, \tag{2.2}$$

$$F'(1) = F(0) = 0, \quad \lim_{r \rightarrow 0} \frac{(F'' - F'/r)}{r} = 0, \quad F(1) = 1. \tag{2.3}$$

As discussed in § 1, a number of asymptotic solutions for F are available for different ranges of R (cf. Terrill & Thomas 1969; Terrill 1983). From Yuan & Finkelstein (1956), two simple solutions that are adequate for either small or large injection can

be expressed as

$$F(r) = \begin{cases} r^2(2 - r^2) + O(10^{-2}Rr^2), & \text{small } R \ (10 < R < 100), \\ \sin(\frac{1}{2}\pi r^2) + O(R^{-1}), & \text{large } R \ (> 100). \end{cases} \tag{2.4}$$

The mean pressure associated with (2.2) can be normalized by γp_s , where γ is the ratio of specific heats, and then integrated from the steady flow momentum equation, $\mathbf{u}_0 \cdot \nabla \mathbf{u}_0 = -M^{-2} \nabla p_0 + \varepsilon \nabla^2 \mathbf{u}_0$. Recalling that $c = \sqrt{(\gamma p_s / \rho_s)}$ and that $p_0(0, 0) = 1/\gamma$, one finds

$$\begin{aligned} p_0 &= \frac{1}{\gamma} - \frac{1}{2} r^{-2} M^2 \{ F^2 + x^2 [F'^2 + (r^{-1} F' - F'')(F - \varepsilon) - \varepsilon r F'''] + \varepsilon r F' \} \\ &= \gamma^{-1} + O(M^2 x^2). \end{aligned} \tag{2.5}$$

Equation (2.5) concurs with the pressure distribution found by Yuan & Finkelstein (1956), Wageman & Guevara (1960) and Durlofsky & Brady (1984). It indicates that the pressure variation in the axial direction is slow, justifying the usage of a constant value over the range $0 < x < 70$. It also explains the finite upper limit posted on the tube length in § 2 a.

(c) *Linearized Navier–Stokes equations*

In normalizing variables, the asterisk is used to designate dimensional quantities. The instantaneous velocity, pressure, density, spatial coordinates and time can be rendered dimensionless via

$$\mathbf{u} = \frac{\mathbf{u}^*}{c}, \quad p \equiv \frac{p^*}{\gamma p_s}, \quad \rho \equiv \frac{\rho^*}{\rho_s}, \quad x = \frac{x^*}{a}, \quad r = \frac{r^*}{a}, \quad t = \frac{t^* c}{a}. \tag{2.6}$$

With this choice of parameters, the Navier–Stokes equations with constant properties can be written as

$$\rho_t + \nabla \cdot (\rho \mathbf{u}) = 0, \tag{2.7}$$

$$\rho [\mathbf{u}_t + (\mathbf{u} \cdot \nabla) \mathbf{u}] = -\nabla p + \varepsilon M \left[\frac{4}{3} \nabla (\nabla \cdot \mathbf{u}) - \nabla \times (\nabla \times \mathbf{u}) \right]. \tag{2.8}$$

In the presence of small oscillations, the total pressure, density and velocity can be expressed as linear sums of steady and temporal fluctuations,

$$p(x, r, t) = 1/\gamma + \bar{\varepsilon} p_1(x, r, t) + O(M^2), \tag{2.9}$$

$$\rho = 1 + \bar{\varepsilon} \rho_1, \quad \mathbf{u} = M \mathbf{u}_0 + \bar{\varepsilon} \mathbf{u}_1, \quad \boldsymbol{\Omega} = M \boldsymbol{\Omega}_0 + \bar{\varepsilon} \boldsymbol{\Omega}_1. \tag{2.10}$$

where $\bar{\varepsilon} = A/(\gamma p_s)$ is the wave amplitude ratio. When the expanded variables are inserted into (2.7) and (2.8), two sets of equations are obtained at $O(1)$ and $O(\bar{\varepsilon})$. While the leading-order set reduces to Berman’s nonlinear equation, the first-order set gives

$$(\rho_1)_t + \nabla \cdot \mathbf{u}_1 = -M \nabla \cdot (\rho_1 \mathbf{u}_0) + O(\bar{\varepsilon}), \tag{2.11}$$

$$\begin{aligned} (\mathbf{u}_1)_t &= -M [\nabla (\mathbf{u}_0 \cdot \mathbf{u}_1) - \mathbf{u}_1 \times \boldsymbol{\Omega}_0 - \mathbf{u}_0 \times \boldsymbol{\Omega}_1] \\ &\quad - \nabla p_1 + \varepsilon M \left[\frac{4}{3} \nabla (\nabla \cdot \mathbf{u}_1) - \nabla \times \boldsymbol{\Omega}_1 \right] + O(\bar{\varepsilon}). \end{aligned} \tag{2.12}$$

In presetting the size of $\bar{\varepsilon}$, we adopt a notion used extensively in classic combustion stability theory, namely, that

$$M^2 < \bar{\varepsilon} < M, \quad \lim_{\bar{\varepsilon}, M \rightarrow 0} \frac{\bar{\varepsilon}}{M} = 0. \tag{2.13}$$

Accordingly, as we reduce M , $\bar{\varepsilon}$ will approach zero more rapidly.

(d) *Irrotational and solenoidal responses*

Using the circumflex and tilde to designate irrotational and solenoidal responses (cf. Majdalani & Roh 2000), one may write

$$\mathbf{u}_1 = \hat{\mathbf{u}} + \tilde{\mathbf{u}}, \quad \text{with } \boldsymbol{\Omega}_1 = \tilde{\boldsymbol{\Omega}}, \quad p_1 = \hat{p} \text{ and } \rho_1 = \hat{\rho}. \tag{2.14}$$

Upon backward substitution into the linearized Navier–Stokes equations, we obtain two distinct sets. The first is the pressure-driven response which can be rearranged into

$$\hat{p}_{tt} - \nabla^2 \hat{p} = -M[\nabla \cdot (\mathbf{u}_0 \hat{p}_t) - \nabla^2(\hat{\mathbf{u}} \cdot \mathbf{u}_0) + \nabla \cdot (\hat{\mathbf{u}} \times \boldsymbol{\Omega}_0)] - \frac{4}{3}\varepsilon M \nabla^2(\nabla \cdot \hat{\mathbf{u}}) + O(\bar{\varepsilon}). \tag{2.15}$$

The second is the vorticity-driven response given by

$$\nabla \cdot \tilde{\mathbf{u}} + O(\bar{\varepsilon}) = 0, \quad \tilde{\mathbf{u}}_t = -M[\nabla(\tilde{\mathbf{u}} \cdot \mathbf{u}_0) - \tilde{\mathbf{u}} \times \boldsymbol{\Omega}_0 - \mathbf{u}_0 \times \tilde{\boldsymbol{\Omega}}] - \varepsilon M \nabla \times \tilde{\boldsymbol{\Omega}} + O(\bar{\varepsilon}). \tag{2.16}$$

Since $\varepsilon M < M$, $\forall \varepsilon < 1$, damping due to viscosity can be ignored at $O(M)$ in (2.15). For longitudinal oscillations, the ensuing pressure and velocity can be written as

$$\left. \begin{aligned} \hat{p}(x, t) &= \cos(\omega_m x) \exp(-i\omega_m t) + O(M), \\ \hat{\mathbf{u}}(x, t) &= i \sin(\omega_m x) \exp(-i\omega_m t) \mathbf{e}_x + O(M), \end{aligned} \right\} \tag{2.17}$$

where $\omega_m = \omega a/c = m\pi/l$, $m = 1, 2, 3, \dots$, for a tube that is acoustically closed at both ends. Solutions corresponding to the closed–open (nozzleless) tube can be obtained straightforwardly by replacing m by $(m - \frac{1}{2})$ everywhere. In much the same way, the oscillatory vortical response can be expressed by

$$\tilde{\mathbf{u}}(x, r, t) = \bar{\mathbf{u}}(x, r) \exp(-i\omega_m t), \quad \tilde{\boldsymbol{\Omega}}(x, r, t) = \bar{\boldsymbol{\Omega}}(x, r) \exp(-i\omega_m t), \tag{2.18}$$

where $\bar{\mathbf{u}} \equiv \bar{u} \mathbf{e}_x + \bar{v} \mathbf{e}_r$ and $\bar{\boldsymbol{\Omega}} \equiv \nabla \times \bar{\mathbf{u}} = \bar{\Omega}_\theta \mathbf{e}_\theta$. Instead of (2.16), we now have

$$\nabla \cdot \bar{\mathbf{u}} + O(\bar{\varepsilon}) = 0, \quad iS\bar{\mathbf{u}} = [\nabla(\bar{\mathbf{u}} \cdot \mathbf{u}_0) - \bar{\mathbf{u}} \times \boldsymbol{\Omega}_0 - \mathbf{u}_0 \times \bar{\boldsymbol{\Omega}}] + \varepsilon \nabla \times \bar{\boldsymbol{\Omega}} + O(\varepsilon M^{-1}), \tag{2.19}$$

where $S = \omega a/V > 10$ is the Strouhal number.

Following Flandro (1995a) and Majdalani & Roh (2000), we now assume that $\bar{v}/\bar{u} = O(M)$. The axial component of (2.19) becomes

$$iS\bar{u} = (u_0 \bar{u})_x + v_0 \bar{u}_r - \varepsilon r^{-1} (r \bar{u}_r)_r. \tag{2.20}$$

(e) *Vorticity and momentum transport formulations*

One may proceed to solve either the vorticity or momentum transport equations. In the first case, one must start by taking the curl of (2.19) to obtain

$$\bar{\Omega}_r - (r^{-1} + iSv_0^{-1})\bar{\Omega} + u_0 v_0^{-1} \bar{\Omega}_x = -\bar{u} v_0^{-1} (\Omega_0)_x + \varepsilon v_0^{-1} (\bar{\Omega}_{xx} + \bar{\Omega}_{rr} + r^{-1} \bar{\Omega}_r - r^{-2} \bar{\Omega}). \tag{2.21}$$

In the second case, \tilde{u} may be derived directly from the momentum equation. To that end, one must first rearrange (2.20) into

$$x\bar{u}_x = \left(\frac{irS}{F'} - 1\right)\bar{u} + \left(\frac{F}{F'}\right)\bar{u}_r + \varepsilon r \frac{(\bar{u}_{rr} + r^{-1}\bar{u}_r)}{F'}. \tag{2.22}$$

Using $\bar{u}(x, r) = X(x)R(r)$ and $\bar{u}(x, 1) = -i\sin(\omega_m x)$, one finds that (2.22) exhibits a solution of the form

$$\bar{u}(x, r) = -i \sum_{n=0}^{\infty} (-1)^n (\omega_m x)^{2n+1} \frac{R_n(r)}{(2n+1)!}, \tag{2.23}$$

where R_n must be solved from

$$\varepsilon \frac{d^2 R_n}{dr^2} + r^{-1}(\varepsilon + F) \frac{dR_n}{dr} + [iS - (2n+2)r^{-1}F']R_n = 0, \quad 0 \leq r \leq 1, \tag{2.24}$$

with

$$R_n(1) = 1 \quad (\text{no-slip}) \quad \text{and} \quad R'_n(0) = 0 \quad (\text{symmetry}). \tag{2.25}$$

By virtue of (2.3), (2.24) admits a regular singularity at the core where $F(0) = 0$. In what follows, both WKB and two-variable multiple-scale expansions will be used to overcome this singularity.

Before initiating the asymptotic work, we define u_1^N as the numerical solution of the linearized momentum equation. It follows that u_1^N can be determined by coupling the numerical solution of (2.24) with (2.23), (2.18) and (2.17).

3. The vorticity-transport technique

(a) Vorticity-transport equation

In this section, (2.21) will be used to derive asymptotic expressions for the rotational vorticity and velocity fields. When $\bar{\Omega} = \varpi_0 + M\varpi_1 + O(M^2)$ is used in (2.21), the leading-order equation becomes

$$(\varpi_0)_r - (r^{-1} + iSv_0^{-1})\varpi_0 + u_0v_0^{-1}(\varpi_0)_x = 0. \tag{3.1}$$

Assuming a solution of the form $\varpi_0 = R(r)X(x)$, one gets

$$\left. \begin{aligned} \varpi_0(x, r) &= r \exp(-i\Phi_0) \sum_{\lambda_n} c_n (xF)^{\lambda_n}, \quad \lambda_n > 0; \\ \Phi_0(r) &= S \int_1^r \frac{x \, dx}{F(x)} = \left\{ \begin{array}{ll} \frac{1}{4}S \ln[r^2/(2-r^2)], & \text{small } R, \\ \frac{1}{\pi}S \ln \tan(\frac{1}{4}\pi r^2), & \text{large } R. \end{array} \right\} \end{aligned} \right\} \tag{3.2}$$

Note that c_n must be specified in a manner to satisfy the no-slip condition at the wall. This condition must be expressed in terms of vorticity. Recalling that $\Omega_1 = \tilde{\Omega}$, $v_1 = \tilde{v}$, $p_1 = \hat{p}$, and that $u_1(x, 1, t)$ must vanish to prevent slippage, the axial projection of (2.12) gives, at the wall,

$$M[(\tilde{v}v_0)_x - \tilde{v}\Omega_0 - v_0\tilde{\Omega}] + \hat{p}_x + \varepsilon M(\tilde{\Omega}_r + r^{-1}\tilde{\Omega}) = 0. \tag{3.3}$$

Rearranging, and using (2.17), one gets

$$\bar{\Omega}(x, 1) = S \sin(m\pi x/l) - \varepsilon(\bar{\Omega}_r + \bar{\Omega}) + O(M). \tag{3.4}$$

(b) Inviscid solution

At the wall, (3.4) must be equated to (3.2) in order to specify the separation eigenvalues. Since $F(1) = 1$ from (2.3), one can write $\varpi_0(x, 1) \equiv S \sin(\omega_m x)$. This will be true when $\lambda_n = 2n + 1$ and

$$c_n = S(-1)^n (\omega_m)^{2n+1} / (2n + 1)! \tag{3.5}$$

Recalling that $\Psi = xF$, backward substitution into (3.2) yields

$$\varpi_0(x, r) = rS \sin(\omega_m \Psi) \exp(-i\Phi_0).$$

Introducing $\bar{u} = r^{-1}\psi_r$ and $\bar{v} = -r^{-1}\psi_x$, the vorticity equation becomes

$$r\bar{\Omega} = -\psi_{xx} + r^{-1}\psi_r - \psi_{rr}. \tag{3.6}$$

When $\psi_0(x, r) = \psi_c(r)\varpi_0(x, r)$ is used in (3.6), a balance between leading-order quantities yields $\psi_c = r\Phi_0'^{-2} = S^{-2}r^{-1}F^2$. Differentiating the stream function for the velocity gives, at length,

$$\bar{\mathbf{u}}(x, r) = -F[i \sin(\omega_m \Psi)\mathbf{e}_x + Mr^{-1}F^2 \cos(\omega_m \Psi)\mathbf{e}_r] \exp(-i\Phi_0). \tag{3.7}$$

(c) Viscous corrections

In order to properly account for viscous effects, we set

$$\bar{\mathbf{u}}(x, r) = u_c(r) \sin(\omega_m \Psi) \exp(-i\Phi_0) \quad \text{and} \quad \bar{\Omega}(x, r) = \varpi_c(r) \sin(\omega_m \Psi) \exp(-i\Phi_0). \tag{3.8}$$

The viscous correction multipliers, u_c and ϖ_c , are then found in a manner to satisfy the complete vorticity-transport equation. In fact, when (3.8) is substituted into (2.21), one notes the cancellation of several terms. Balancing the remaining quantities requires that

$$\frac{d\varpi_c}{dr} - (\varepsilon S^2 r^3 F^{-3} + r^{-1})\varpi_c + (F'' - F'r^{-1})F^{-1}u_c = 0. \tag{3.9}$$

At this point, a relation between u_c and ϖ_c is needed to make any headway. Defining $\xi \equiv \varepsilon S^2 = a\nu\omega^2 V^{-3}$, we realize that $10^{-2} < \xi < 10^2$, $10^{-1} < \varepsilon^{1/2}S < 10$, $S = O(\varepsilon^{-1/2})$ and $S \sim \sqrt{R}$. Next we use (2.20) and find that

$$u_c = -S^{-1}(iF'r^{-1} + \xi S^{-1}rF^{-1})\varpi_c.$$

Inserting this expression into (3.9) leads to

$$\frac{d\varpi_c}{dr} - [\xi r^3 F^{-3} + r^{-1} + iS^{-1}r^{-1}(F'' - r^{-1}F')] \varpi_c = 0, \quad \varpi_c(r) = Cr \exp \zeta_0, \tag{3.10}$$

where

$$\begin{aligned} \frac{\zeta_0}{\xi} &= \int_1^r x^3 F^{-3}(x) dx \\ &= \begin{cases} -\frac{1}{32}[3 \ln(2r^{-2} - 1) + 2(1 - r^{-2})(2r^4 - 3r^2 - 4)(2 - r^2)^{-2}], & \text{small } R, \\ -\pi^{-2}[\csc \theta + \theta \cot \theta \csc \theta - 1 - I(\theta) + I(\frac{1}{2}\pi)], & \theta \equiv \frac{1}{2}\pi r^2, \text{ large } R, \end{cases} \end{aligned} \tag{3.11}$$

and

$$\begin{aligned}
 I(x) &= x + \sum_{k=1}^{\infty} (-1)^k \frac{2(1 - 2^{2k-1})B_{2k}x^{2k+1}}{(2k + 1)!} \\
 &= x + \frac{1}{18}x^3 + \frac{7}{1800}x^5 + \frac{31}{105840}x^7 + \dots
 \end{aligned}
 \tag{3.12}$$

The integration constant C in (3.10) can be specified from (3.4). Noting that $\zeta'_0(1) = \xi$, $\Phi'_0(1) = S$ and $\zeta_0(1) = \Phi_0(1) = 0, \forall F$, we find $C(1 - i\varepsilon S) = S + O(S^{-2})$. Hence,

$$C^r = \frac{S}{1 + \varepsilon^2 S^2} \quad \text{and} \quad C^i = \frac{\varepsilon S^2}{1 + \varepsilon^2 S^2}.
 \tag{3.13}$$

Straightforward substitution into (3.10), (3.8) and (2.18) yields

$$\bar{\Omega} = Cr \sin(\omega_m \Psi) \exp(\zeta_0 - i\Phi_0 - i\omega_m t).$$

The corrective multiplier is therefore

$$u_c = -S^{-1}(ir^{-1}F + \varepsilon SrF^{-1})Cr \exp \zeta_0 \equiv iUr \exp \zeta_0,$$

where

$$U^r = -S^{-1}C^r r^{-1}F - \varepsilon C^i r F^{-1} \quad \text{and} \quad U^i = \varepsilon C^r r F^{-1} - S^{-1}C^i r^{-1}F,
 \tag{3.14}$$

Next, \tilde{u} may be obtained from (3.8) and (2.18). The outcome is

$$\tilde{u} = irU \sin(\omega_m \Psi) \exp(\zeta_0 - i\Phi_0 - i\omega_m t).$$

Having fully determined \tilde{u} , \tilde{v} can be obtained, at leading order, from mass conservation. Starting with $\tilde{v} = r^{-1}g(r) \cos(\omega_m \Psi) \exp(\zeta_0 - i\Phi_0 - i\omega_m t)$, substitution into $r^{-1}(r\tilde{v})_r + \bar{u}_x = 0$ requires that $g = MrUF^2$. Using the superscript ‘V’ for the vorticity-transport formulation, key results obtained heretofore can be summarized in

$$\left. \begin{aligned}
 u_1^V &= \sin(\omega_m x) \sin(\omega_m t) - r(U^r \sin \varphi - U^i \cos \varphi) \exp \zeta_0 \sin(\omega_m x F), \\
 \varphi &= \omega_m t + \Phi_0,
 \end{aligned} \right\}
 \tag{3.15}$$

$$\left. \begin{aligned}
 v_1^V &= MF^2(U^r \cos \varphi + U^i \sin \varphi) \exp \zeta_0 \cos(\omega_m x F), \\
 \Omega_1^V &= (C^r \cos \varphi + C^i \sin \varphi)r \exp \zeta_0 \sin(\omega_m x F).
 \end{aligned} \right\}
 \tag{3.16}$$

4. The WKB technique

(a) The WKB expansion

Formal WKB theory (cf. Bender & Orszag 1978) suggests setting

$$R_n(r) = \exp(\delta^{-1}S_0 + S_1 + \delta S_2 + \delta^2 S_3 + \delta^3 S_4 + \dots),
 \tag{4.1}$$

where δ is a small parameter and $S_j(r)$ must be determined sequentially for $j \geq 0$. Straightforward differentiation and substitution into (2.24) yields the distinguished limit $\delta = \sqrt{\varepsilon}$ and $S\sqrt{\varepsilon} = O(1)$. The equation for S_0 becomes

$$Fr^{-1}S'_0 + iS\sqrt{\varepsilon} = 0, \quad S_0(1) = 0 \quad \Rightarrow \quad S_0(r) = -iS\sqrt{\varepsilon} \int_1^r xF^{-1}(x) dx = -i\sqrt{\varepsilon}\Phi_0.
 \tag{4.2}$$

By the same token, one finds

$$Fr^{-1}S'_1 + S_0'^2 - (2n + 2)F'r^{-1} = 0, \quad S_1(1) = 0 \tag{4.3}$$

hence

$$S_1(r) = (2n + 2) \ln F + \xi \int_1^r x^3 F^{-3}(x) dx. \tag{4.4}$$

$$Fr^{-1}S'_2 + S_0'' + 2S_0'S'_1 + r^{-1}S_0' = 0, \quad S_2(1) = 0, \tag{4.5}$$

and so

$$S_2(r) = iS\sqrt{\varepsilon} \left\{ (2n + \frac{3}{2})[1 - r^2 F^{-2}(r)] + (4n + 5) \int_1^r x F^{-2} dx + 2\xi \int_1^r x^5 F^{-5} dx \right\}. \tag{4.6}$$

The first-order WKB solution can be constructed via (4.1). Using ‘W’ for WKB, one may write

$$R_n^W(r) = F^{2n+2} \exp(\zeta_0 - i\Phi_0 - i\Phi_1^n) + O(\varepsilon), \tag{4.7}$$

with

$$\Phi_1^n \equiv -\varepsilon S \left\{ (2n + \frac{3}{2})[1 - r^2 F^{-2}(r)] + (4n + 5) \int_1^r x F^{-2} dx + 2\xi \int_1^r x^5 F^{-5} dx \right\}. \tag{4.8}$$

For small and large R , Φ_1^n can be calculated from

$$\frac{\Phi_1^n}{\varepsilon S} = \begin{cases} \frac{1}{128} r^{-4} (2 - r^2)^{-4} \\ \times [32\xi + 2r^2(16(2 - r^2)^2(1 - r^2)[16(1 + n) - (23 + 28n)r^2 + 2(3 + 4n)r^4] \\ + \xi\{48 + r^2[6 - r^2(3 - r^2)(84 - 65r^2 + 16r^4)\}] \\ + r^4(2 - r^2)^4(80 + 64n + 15\xi) \ln(2r^{-2} - 1)], \text{ small } R \\ \pi^{-1} \{(4n + 5) \cot \theta + (4n + 3)(\theta \csc^2 \theta - \frac{1}{2}\pi) - 8\pi^{-2}\xi[T(\theta) - T(\frac{1}{2}\pi)]\}, \\ \text{large } R, \end{cases} \tag{4.9}$$

where

$T(x)$

$$\begin{aligned} &= \int x^2 \csc^5 x dx \\ &= \frac{1}{48} \{40 \ln \tan(\frac{1}{2}x) + 9x^2 - 2 \csc x [18x + (2 + 9x^2) \cot x] - 4x \csc^3 x (2 + 3x \cot x)\} \\ &\quad + \frac{3}{4} \sum_{k=1}^{\infty} (-1)^k \frac{(1 - 2^{2k-1}) B_{2k} x^{2k+2}}{(2k + 2)(2k)!}. \end{aligned} \tag{4.10}$$

(b) The first-order WKB solution

Equation (4.7) can be inserted back into (2.23) to render

$$\begin{aligned} \bar{u}(x, r) &= -iF \exp(\zeta_0 - i\Phi_0 - i\Phi_1^n) \sum_{n=0}^{\infty} \frac{(-1)^n (\omega_m x F)^{2n+1}}{(2n + 1)!} \\ &= -iF \exp(\zeta_0 - i\Phi_0 - i\Phi_1^n) \sin(\omega_m x F). \end{aligned} \tag{4.11}$$

This formula can be used in conjunction with (2.18), (2.17) and (2.14) to construct the oscillatory velocity component. At length, one finds

$$u_1^W(x, r, t) = \sin(\omega_m x) \sin(\omega_m t) - F \sin(\omega_m x F) \exp \zeta^W \sin(\omega_m t + \Phi^W); \tag{4.12}$$

$$\left. \begin{aligned} \zeta^W &= \zeta_0, & \Phi^W &= \Phi_0 + \Phi_1^0, \\ \Phi_1^0 &= -\varepsilon S \left\{ \frac{3}{2} [1 - r^2 F^{-2}(r)] + 5 \int_1^r x F^{-2} dx + 2\xi \int_1^r x^5 F^{-5} dx \right\}, \end{aligned} \right\} \tag{4.13}$$

wherein

$$\Phi_1^0 = \begin{cases} \frac{1}{128} \varepsilon S [r^4 (2 - r^2)^4 (80 + 15\xi) \ln(2r^{-2} - 1) \\ \quad + 2r^2 (16(2 - r^2)^2 (1 - r^2) (16 - 23r^2 + 6r^4) \\ \quad + \xi \{ 48 + r^2 [6 - r^2 (3 - r^2) (84 - 65r^2 + 16r^4) \}] \\ \quad + 32\xi] r^{-4} (2 - r^2)^{-4}, & \text{small } R, \\ \pi^{-1} \varepsilon S \{ 5 \cot \theta + 3(\theta \csc^2 \theta - \frac{1}{2}\pi) - 8\pi^{-2} \xi [T(\theta) - T(\frac{1}{2}\pi)] \}, & \text{large } R. \end{cases} \tag{4.14}$$

5. The undetermined-scale technique

(a) *Nonlinear transformation*

A two-variable expansion requires specifying two fictitious coordinates, an outer scale, r_0 , and an inner scale, r_1 . Conventional scaling transformations include variable selections of the form $r_1 = f(\varepsilon)r$, or $r_1 = f(\varepsilon)(1 - r)$. According to formal practices, the strict definition of $f(\varepsilon)$ must precede the expansion. The difficulty, in our case, is that conventional selections fail to yield uniformly valid solutions. In fact, we find it necessary to introduce a nonlinear variable transformation of the form $r_1 = \varepsilon s(r)$. Our choice is different in that $s(r)$ is not pre-set by foreknowledge, rationalization, or an order-of-magnitude analysis. Rather, it is left to be an undetermined function that can accommodate generally nonlinear distortions. This choice provides more freedom and enables us to determine $s(r)$ in a manner to satisfy the problem's solvability condition. The latter can be rigorously prescribed using either Prandtl's principle of matching by supplementary expansions, or the principle of least singular behaviour.

(b) *The two-scale expansion*

Introducing $r_0 = r$ and $r_1 = \varepsilon s(r)$, functions and derivatives can be expanded in a manner to discard $O(\varepsilon^2)$ quantities. Using superscripts to denote perturbation orders, one can write

$$\left. \begin{aligned} R_n(r_0, r_1) &= R^{(0)}(r_0, r_1) + \varepsilon R^{(1)}(r_0, r_1) + O(\varepsilon^2), \\ \frac{d}{dr} &= \frac{\partial}{\partial r_0} + \varepsilon \frac{ds}{dr_0} \frac{\partial}{\partial r_1}, & \frac{d^2}{dr^2} &= \frac{\partial^2}{\partial r_0^2} + O(\varepsilon). \end{aligned} \right\} \tag{5.1}$$

Inserting these expansions into (2.24), terms of the same power in ε can be collected. The result is

$$\frac{\partial R^{(0)}}{\partial r_0} + \left[i \frac{r_0 S}{F} - 2(n+1) \frac{F'}{F} \right] R^{(0)} = 0, \quad R^{(0)}(1) = 1, \quad \frac{\partial R^{(0)}}{\partial r_0}(0) = 0, \quad (5.2)$$

$$\frac{\partial R^{(1)}}{\partial r_0} + \left[i \frac{r_0 S}{F} - 2(n+1) \frac{F'}{F} \right] R^{(1)} = - \frac{ds}{dr_0} \frac{\partial R^{(0)}}{\partial r_1} - \frac{1}{F} \frac{\partial R^{(0)}}{\partial r_0} - \frac{r_0}{F} \frac{\partial^2 R^{(0)}}{\partial r_0^2}. \quad (5.3)$$

Since $F(1) = 1$ is a property of all Berman functions, integration of the leading-order equation yields

$$R^{(0)}(r_0, r_1) = a_1(r_1) \exp \left[2(n+1) \ln F(r_0) - iS \int_1^{r_0} x F^{-1}(x) dx \right]. \quad (5.4)$$

Here, a_1 must be determined in a manner to ensure a secular-free series expansion of R_n . This can be achieved when the right-hand side of (5.3) is set to zero. The resulting first-order differential equation in a_1 can be integrated in closed form (using $\eta(1) = 0$, $R_n(1) = 1$ and $s(1) = 0$). Expressed in the original laboratory coordinate, one obtains

$$a_1 = \exp(-\xi \eta r^3 F^{-3} \{ 1 - 2S^{-2}(n+1)r^{-2}[F(F'' + r^{-1}F') + (2n+1)F'^2] + iS^{-1}r^{-2}[rF'(4n+3) + 2F] \}). \quad (5.5)$$

The effective scale functional $\eta(r)$ that appears in (5.5) is

$$\eta(r) \equiv -s(r)/s'(r). \quad (5.6)$$

Knowing $\eta(r)$, the rest is straightforward substitution into (5.4). Recalling that the overall solution is sought at $O(\varepsilon M^{-1})$, retention of $R^{(0)}$ is sufficient. Subsequently, (5.1) becomes

$$R_n = F^{2n+2} \exp \left(-\xi \eta r^3 F^{-3} - iS \left\{ \int_1^r x F^{-1} dx + \xi S^{-2} r \eta F^{-3} [rF'(4n+3) + 2F] \right\} \right) + O(\varepsilon). \quad (5.7)$$

(c) Prandtl's principle of matching by supplementary expansions

Based on Prandtl's principle of matching by supplementary functions, the undetermined-scale solution developed here must exhibit the same leading-order terms obtained using the basic WKB expansion. Physically, the spatial damping function in (5.7) must match its counterpart arising in the WKB solution. This will be the case when

$$\begin{aligned} \eta^U(r) &= -r^{-3} F^3(r) \int_1^r x^3 F^{-3}(x) dx \\ &= \begin{cases} \frac{1}{32} r^3 (2-r^2)^3 \left\{ \ln \frac{(2-r^2)^3}{r^6} + 4 + \frac{2[4+3r^2(r^2-3)]}{r^2(2-r^2)^2} \right\}, & \text{small } R, \\ \pi^{-2} [\csc \theta + \theta \cot \theta \csc \theta - 1 + I(\frac{1}{2}\pi) - I(\theta)] r^{-3} \sin^3 \theta, & \text{large } R. \end{cases} \end{aligned} \quad (5.8)$$

As usual, the superscript ‘U’ is used to denote the result based on the undetermined-scale technique. Having determined η^U , the undetermined coordinate transformation can be specified from (5.6). The result is

$$s^U(r) \sim \int_1^r x^3 F^{-3}(x) dx. \tag{5.9}$$

Equation (5.9) is a key expression that unravels the dependence of $s(r)$ on the Berman function F . The algebraic content of (5.9) may be the reason for the futility of standard multiple-scale methods.

(d) *The undetermined-scale solution*

Having determined R_n , (5.7) can be substituted into (2.23) and (2.18), and then added to (2.17). One gets

$$\begin{aligned} u_1(x, r, t) = & -iF \sum_{n=0}^{\infty} \frac{(-1)^n (\omega_m x F)^{2n+1}}{(2n+1)!} \\ & \times \exp\left(-\xi \eta r^3 F^{-3} \right. \\ & \left. - iS \left\{ \int_1^r x F^{-1} dx + \xi S^{-2} r \eta F^{-3} [r F'(4n+3) + 2F] \right\} - i\omega_m t \right) \\ & + i \sin(\omega_m x) \exp(-i\omega_m t) + O(\varepsilon). \end{aligned} \tag{5.10}$$

Since the error associated with $n \geq 1$ terms is smaller than the error at $n = 0$, corrections of $O(S^{-2})$ can be retained for $n = 0$ and dismissed for $n \geq 1$. The equivalent expression for u_1 is

$$\begin{aligned} u_1 = & i \exp(-i\omega_m t) \left(\sin(\omega_m x) - F \sin(\omega_m x F) \exp\left\{ -\xi \eta r^3 F^{-3} \right. \right. \\ & \left. \left. - iS \left[\int_1^r x F^{-1} dx + \varepsilon r \eta F^{-3} (3r F' + 2F) \right] \right\} \right). \end{aligned} \tag{5.11}$$

The meaningful part of the solution is identical to (4.12), namely,

$$u_1^U(x, r, t) = \sin(\omega_m x) \sin(\omega_m t) - F \sin(\omega_m x F) \exp \zeta^U \sin(\omega_m t + \Phi^U), \tag{5.12}$$

where

$$\left. \begin{aligned} \zeta^U = \zeta_0 = & -\xi \eta^U r^3 F^{-3}, \\ \Phi^U = \Phi_0 + \Phi_1 = & S \left[\int_1^r x F^{-1} dx + \varepsilon r \eta^U F^{-3} (3r F' + 2F) \right]. \end{aligned} \right\} \tag{5.13}$$

(e) *Total solution*

From the axial component \tilde{u} , the radial velocity \tilde{v} can be obtained by appealing to continuity. To expedite the process, one may let

$$\tilde{v}(x, r, t) = r^{-1} G(r) \cos(\omega_m x F) \exp \zeta \exp[-i(\omega_m t + \Phi)], \tag{5.14}$$

where $G(r)$ is a subsidiary function that must be determined so that $\tilde{u}_x + r^{-1}(r\tilde{v})_r = 0$. After some algebra, we find that $G = -MF^3$. By differentiating \tilde{u} and \tilde{v} , the temporal vorticity is also obtainable. The total periodic components become

$$\left. \begin{aligned} v_1^U(x, r, t) &= -Mr^{-1}F^3 \cos(\omega_m x F) \exp \zeta^U \cos(\omega_m t + \Phi^U), \\ \Omega_1^U &= rS \sin(\omega_m x F) \exp \zeta^U \cos(\omega_m t + \Phi^U). \end{aligned} \right\} \quad (5.15)$$

Despite their dissimilar expressions, both v_1^U and Ω_1^U agree, almost to a fault, with (3.16).

6. The generalized-scale technique

(a) Nonlinear transformation

In the previous section, the modified variable is left unspecified while carrying out the two-scale expansion. At the conclusion of the asymptotic analysis, physical arguments are employed to evaluate the required transformation. These physical arguments are based on comparisons with the basic WKB solution. Despite the novelty in retaining an undetermined scale throughout the derivation process, the main limitation plaguing the previous approach lies in its strict dependence on the availability of an alternative approximation. This limitation is caused by Prandtl’s principle requiring the presence of at least one other expansion for the same problem.

The main purpose of this section is to present a different approach that leads to the independent specification of the inner scaling transformation. This will be obtained by imposing the problem’s solvability condition stemming from the principle of minimum singularity. At the outset, the generally nonlinear scale will be determined by satisfying the mathematical constraint requiring boundedness between successive asymptotic orders. Unlike the former solutions, the current procedure precludes guessing and reveals, totally independently, the problem’s intrinsic scales.

(b) The generalized two-scale expansion

As before, we let $R_n(r_0, r_1) = R^{(0)}(r_0, r_1) + \varepsilon R^{(1)}(r_0, r_1) + O(\varepsilon^2)$, where $r_0 = r$ and $r_1 = \varepsilon s(r)$. The only difference here is that the general transformation will have to originate from the problem’s solvability condition. The leading-order solution can be readily put in the form

$$R^{(0)}(r_0, r_1) = C_1(r_1) \exp \left[2(n + 1) \ln F(r_0) - iS \int_1^{r_0} x F^{-1}(x) dx \right], \quad (6.1)$$

where C_1 awaits evaluation from the first-order equation. This corrective multiplier must be determined in a manner to promote the least singular behaviour in R_n . To that end, we find it unnecessary to determine $R^{(1)}$ fully. In fact, it will be sufficient to formulate a solvability condition for which an asymptotic series of the form $R^{(0)} + \varepsilon R^{(1)} + o(\varepsilon)$ can exist. This may be accomplished by first introducing

$$\Pi = \frac{R^{(1)}(r_0, r_1)}{R^{(0)}(r_0, r_1)}. \quad (6.2)$$

In order to determine Π , one can multiply (5.2) by $R^{(1)}[R^{(0)}]^{-2}$ and subtract the result from the product of (5.3) and $[R^{(0)}]^{-1}$. One gets

$$\frac{1}{R^{(0)}} \frac{\partial R^{(1)}}{\partial r_0} - \frac{R^{(1)}}{[R^{(0)}]^2} \frac{\partial R^{(0)}}{\partial r_0} = -\frac{s'}{R^{(0)}} \frac{\partial R^{(0)}}{\partial r_1} - \frac{1}{FR^{(0)}} \frac{\partial R^{(0)}}{\partial r_0} - \frac{r_0}{FR^{(0)}} \frac{\partial^2 R^{(0)}}{\partial r_0^2}. \tag{6.3}$$

Noting that the left-hand side is the derivative of Π , (6.3) can be written as

$$\begin{aligned} \frac{\partial \Pi}{\partial r_0} &= \frac{\partial}{\partial r_0} \left[\frac{R^{(1)}}{R^{(0)}} \right] \\ &= -\frac{s'}{C_1} \frac{dC_1}{dr_1} + S^2 r_0^3 F^{-3} - 2(n+1)F'F^{-2} - 2(n+1)r_0 F''F^{-2} \\ &\quad - 2(n+1)(2n+1)r_0 F'^2 F^{-3} + iS r_0 F^{-2} + i(4n+3)S r_0^2 F'F^{-3}. \end{aligned} \tag{6.4}$$

Therefore,

$$\begin{aligned} \Pi &= -\frac{s}{C_1} \frac{dC_1}{dr_1} \\ &\quad + S^2 \int_1^{r_0} \{x^3 F^{-3} - 2(n+1)S^{-2}[F'F^{-2} + xF''F^{-2} + (2n+1)xF'^2 F^{-3}] \\ &\quad \quad \quad + iS^{-1}xF^{-2}[1 + (4n+3)xF'F^{-1}]\} dx. \end{aligned} \tag{6.5}$$

(c) *The problem's solvability condition*

In order to promote a uniformly valid asymptotic series, the ratio of $R^{(1)}$ and $R^{(0)}$ must be bounded $\forall r_1$. This can be accomplished by imposing $\Pi = O(1)$. For arbitrary F , Π will be bounded $\forall r_1$ if

$$\left. \begin{aligned} \frac{1}{C_1(r_1)} \frac{dC_1(r_1)}{dr_1} &\equiv K(r_1) = O(1) \quad \text{or} \\ C_1 &= C_0 \exp\left(\int K dr_1\right) = C_0 \exp\left(\varepsilon \int K ds\right). \end{aligned} \right\} \tag{6.6}$$

Here C_0 is a constant that can be later determined from $R^{(0)}(1) = 1$. Setting $K = \text{const.}$ will be sufficient (but not necessary) to guarantee boundedness. In fact, $K(r_1)$ will prove to be important for temporary bookkeeping. From (6.5), one finds

$$\begin{aligned} s &= K^{-1} S^2 \left(\int_1^{r_0} \{x^3 F^{-3} - 2(n+1)S^{-2}F^{-2}[F' + xF'' + (2n+1)xF'^2 F^{-1}] \right. \\ &\quad \quad \quad \left. + iS^{-1}xF^{-2}[1 + (4n+3)xF'F^{-1}]\} dx - S^{-2}\Pi \right). \end{aligned} \tag{6.7}$$

Recalling that $\Pi = O(1)$, one can put

$$s = K^{-1} S^2 \left(\int_1^{r_0} \{x^3 F^{-3} + iS^{-1}xF^{-2}[1 + (4n+3)xF'F^{-1}]\} dx + O(S^{-2}) \right). \tag{6.8}$$

At this point, small corrections of $O(S^{-2} \sim \varepsilon)$ can be ignored. Partial differentiation of (6.8) gives

$$\frac{\partial s}{\partial r_0} = K^{-1} S^2 \{r_0^3 F^{-3} + i S^{-1} r_0 F^{-2} [1 + (4n + 3)r_0 F' F^{-1}]\}. \tag{6.9}$$

When (6.9) is paired with (5.1), it can be seen that

$$\begin{aligned} ds &= \left(\frac{\partial s}{\partial r_0} + \varepsilon s' \frac{\partial s}{\partial r_1} \right) dr \\ &= (K^{-1} S^2 \{r_0^3 F^{-3} + i S^{-1} r_0 F^{-2} [1 + (4n + 3)r_0 F' F^{-1}]\} + O(\varepsilon)) dr. \end{aligned} \tag{6.10}$$

(d) The generalized-scale solution

In the process of substituting (6.10) back into (6.6), K is fully eliminated. One is left with

$$C_1 = C_0 \exp\left(\varepsilon \int S^2 \{r^3 F^{-3} + i S^{-1} r F^{-2} [1 + (4n + 3)r F' F^{-1}]\} dr\right). \tag{6.11}$$

Further substitution into (6.1) gives the leading-order solution

$$R_n = F^{2n+2} \exp\left(\int_1^r \{\xi x^3 F^{-3} - i S [x F^{-1} - \varepsilon x F^{-2} - (4n + 3)\varepsilon x^2 F' F^{-3}]\} dx\right), \tag{6.12}$$

where the boundary condition $R_n(1) = 1$ has been applied. Using $x^2 F' F^{-3} = (-\frac{1}{2} x F^{-2})' + x F^{-2}$, one simplifies (6.12) into

$$\begin{aligned} R_n^G &= F^{2n+2} \exp\left[\int_1^{r_0} \{\xi x^3 F^{-3} - i S [x F^{-1} - 4(n + 1)\varepsilon x F^{-2}]\} dx \right. \\ &\quad \left. + i(2n + \frac{3}{2})\varepsilon S(1 - r^2 F^{-2})\right] + O(\varepsilon). \end{aligned} \tag{6.13}$$

In the above, ‘G’ denotes a multiple-scale solution based on a generalized coordinate. The current solution can be expressed in the same form as (5.12) and (5.15). The difference here is that Φ^G must be replaced by

$$\Phi^G = S \left[\int_1^r (x F^{-1} - 4\varepsilon x F^{-2}) dx + \frac{3}{2}\varepsilon(r^2 F^{-2} - 1) \right]; \tag{6.14}$$

$$\Phi^G = \begin{cases} -\frac{1}{4} S [(1 - 2\varepsilon) \ln(2r^{-2} - 1) + 2\varepsilon(1 - r^{-2})(7 - 11r^2 + 3r^4)(2 - r^2)^{-2}], & \text{small } R, \\ S\pi^{-1} \{\ln \tan(\frac{1}{2}\theta) + \varepsilon[4 \cot \theta + 3(\theta \csc^2 \theta - \frac{1}{2}\pi)]\}, & \text{large } R. \end{cases} \tag{6.15}$$

(e) The general characteristic length

In the current analysis, determination of η is not a prerequisite for finding $s(r)$. Specification of the generalized scale in (6.8) is done exclusively by observing the principle of minimum singularity. From (6.8), the need for a nonlinear coordinate

transformation is explicitly ascertained. Although unnecessary, the problem's characteristic length-scale can be evaluated from (5.6), (6.8) and (6.10). One finds

$$\eta^G(r) \sim \frac{-r^{-3}F^3 \int_1^r x^3 F^{-3} \{1 + iS^{-1}x^{-3}[xF + (4n+3)x^2F']\} dx}{\{1 + iS^{-1}r^{-3}[rF + (4n+3)r^2F']\}}, \quad (6.16)$$

which confirms that

$$s^G(r) \sim \int_1^r \{x^3F^{-3} + iS^{-1}xF^{-2}[1 + (4n+3)xF'F^{-1}]\} dx. \quad (6.17)$$

It is interesting to note that η^U can be restored from η^G since $\eta^G \rightarrow \eta^U$ as $S \rightarrow \infty$, $\forall n$. Thus η^U in (5.8) represents the dominant, leading-order part of η^G . Similarly, s^U in (5.9) is recoverable from s^G . This may explain the ability of the undetermined-scale technique to yield a uniformly valid approximation.

7. Other approximations

(a) The composite-scale technique

In two previous studies, Majdalani & Van Moorhem (1995, 1998) used a different approach to analyse the large injection problem. Following a space-reductive multiple-scale theory, inner, outer and intermediate scales were first identified and then replaced by one 'composite' function, $s^C(r) = (1-r)r^{-a(1-r)^b}$, with $a = b = \frac{3}{2}$. The composite scale s^C was uniformly valid over the solution domain and could reproduce asymptotically the scales that existed near $r = 0, 1$. The corresponding η could be derived by direct differentiation of s^C . The resulting functional, namely,

$$\eta^C(r) = (1-r)\{1 + a(1-r)^b[(1-r)r^{-1} - b \ln r]\}^{-1}, \quad (7.1)$$

was corroborated by Majdalani (1998) in a separate study covering the porous channel flow. For small injection, one finds $a = \frac{4}{3}$ and $b = \frac{8}{3}$. The composite-scale solution can now be reproduced by simply substituting η^C into (5.12) and (5.13).

(b) Zhao's approximation

In similar but independent work concerned with large sidewall injection in a tube, Zhao *et al.* (2000) introduced a nonlinear transformation also. However, Zhao's transformation was based on the choice of two scales that were found by intuition. While the first scale was taken to be the radial distance from the wall, the second was based on a 'much shorter length associated with the radial distance travelled by a fluid particle on the acoustic timescale.' Subject to a minor correction in the lower bound of Zhao's defining integral (i.e. the lower bound should be '1' instead of '0' lest the nonlinear scale be indeterminate), the two scales introduced by Zhao are

$$r_1 = 1 - r \equiv y \quad \text{and} \quad r_2 = M^{-1}V^{-1}(x) \int_1^{r_1} z \csc\left(\frac{1}{2}\pi z^2\right) dz. \quad (7.2)$$

Here $V(x)$ represents the normalized radial velocity distribution along the porous walls. For uniform injection, $V(x) = 1$. The scaling transformation employed by

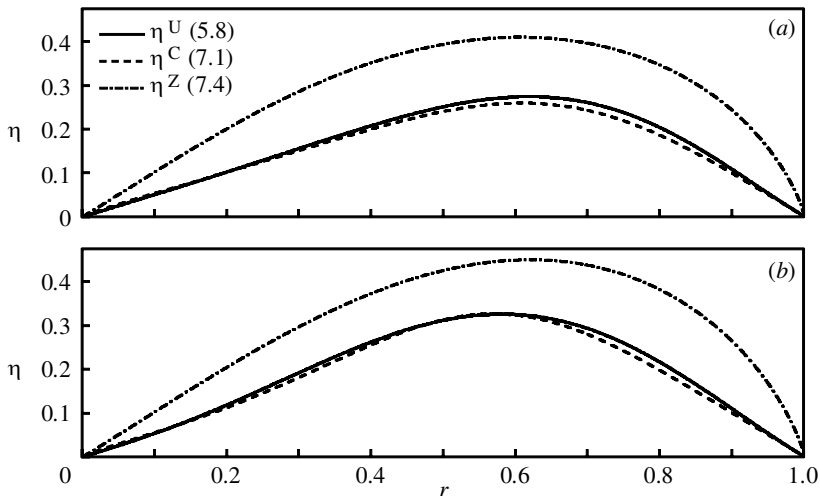


Figure 2. Comparing the characteristic length-scale η^U with existing theories for (a) large and (b) small crossflow Reynolds numbers. While η^C is the composite length-scale derived by Majdalani & Van Moorhem (1995), η^Z is based on the scales introduced by Zhao *et al.* (2000).

Zhao *et al.* (2000) can be extended to a problem with arbitrary injection. For that purpose, one must have

$$\left. \begin{aligned} r_1 &= 1 - r, \\ r_2 &= M^{-1}V^{-1}(x) \int_1^{r_1} \frac{z \, dz}{F(z)} = \begin{cases} \frac{1}{4}M^{-1}V^{-1}(x) \ln[y^2/(2 - y^2)], & \text{small } R, \\ \pi^{-1}M^{-1}V^{-1}(x) \ln \tan(\frac{1}{4}\pi y^2), & \text{large } R. \end{cases} \end{aligned} \right\} \quad (7.3)$$

Using ‘Z’ to denote the scale functional based on the idea presented by Zhao *et al.* (2000), one finds

$$\eta^Z = y^{-1}F(y) \int_1^y \frac{z \, dz}{F(z)} = \begin{cases} \frac{1}{4}y(2 - y^2) \ln[y^2/(2 - y^2)], & \text{small } R, \\ \pi^{-1}y^{-1} \sin(\frac{1}{2}\pi y^2) \ln \tan(\frac{1}{4}\pi y^2), & \text{large } R. \end{cases} \quad (7.4)$$

At this point, Zhao’s approximation can be obtained by substituting η^Z into (5.12) and (5.13).

8. Results and discussion

(a) Characteristic length-scales

So far, several nonlinear length-scales have been presented. Physically, η^G , η^U , η^C and η^Z represent approximations to the characteristic length-scale for radial convection and attenuation of rotational disturbances. The intrinsic nonlinearity of η can be attributed to the co-existence of three important mechanisms evolving simultaneously on vastly dissimilar dimensions. These are viscous diffusion, radial convection and unsteady inertia. While viscous forces diffuse vorticity on the small Stokes length, $\sqrt{2\nu/\omega}$, radial convection of unsteady vorticity evolves on a spatially varying wavelength. By analogy to the channel flow analysis (Majdalani & Roh 2000), the

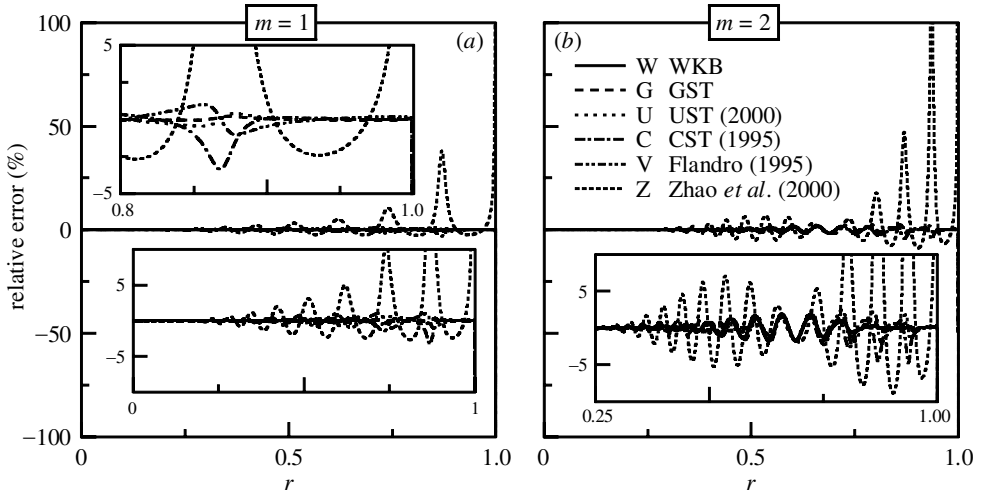


Figure 3. Error entailed in the various asymptotic formulations for u_1^W , u_1^G , u_1^U , u_1^C , u_1^V and u_1^Z . For the first two oscillation modes, we compare solutions for a typical cold-flow experiment with $S = 50m$ and $R = 5000$. Results are presented at acoustic pressure nodes corresponding to (a) $x/l = \frac{1}{2}$ and (b) $x/l = \frac{3}{4}$. Relative deviations from the numerical solution appear to be contained within $\pm 5\%$ at the exception of u_1^Z . Enlargements are shown in the insets.

dimensional wavelength for radial propagation of vorticity waves can be shown to be $2\pi VF/(\omega r)$.

On the one hand, both η^G and η^U are systematically determined *a posteriori* without the need for guessing. While η^U obeys Prandtl's principle of matching by supplementary functions, η^G is derived from the coordinate transformation prescribed by the principle of minimum singularity. Due to the validity of both principles, it is not surprising that η^U can be recovered from η^G for large S . On the other hand, both η^C and η^Z are introduced at the beginning of the asymptotic analysis. While η^C requires repeated trials to identify the inner scales, η^Z is obtained following a rough scaling analysis. Despite the different modes of analysis used in their determination, these scales exhibit interesting similarities. Figure 2 illustrates their behaviour for both large and small injections. Graphically, η^U and η^C seem to exhibit the same algebraic content despite their completely dissimilar expressions. Despite matching the endpoints at $r = 0, 1$, the appreciating discrepancy between η^Z and the formal scales can be attributed to the dependence of η^Z on F instead of F^3 . This may also explain the reduced precision that can be associated with Zhao's approximation.

It should be noted that the idea of a nonlinear scale is not entirely novel. It has been reported by Van Dyke (1975) that a nonlinear transformation had been first introduced by Munson (1964). The relevant work involved the convection–diffusion equation appropriate to the study of the vortical layer on an inclined cone. In that problem, linear stretching was ineffective, and an inner coordinate of the form $r_1 = r^\epsilon$ had to be devised. The main novelty in the current analysis lies, perhaps, in the manner by which the scales are derived, *a posteriori*, by appealing to fundamental principles.

Table 1. Temporal velocity comparisons for a typical cold flow experiment with $S = 50m$, $\xi = \frac{1}{2}m^2$, $R = 5000$, $\omega_m t = \frac{1}{2}\pi$, $x/l = \frac{1}{2}$ and $m = 1$

r	u_1^N	u_1^W	u_1^G	u_1^U
0.25	1.004 653 1	1.004 477 4	1.003 932 8	1.004 351 4
0.30	1.006 703 5	1.006 608 7	1.005 142 5	1.006 438
0.35	0.973 365 10	0.973 743 5	0.972 463 2	0.973 761 7
0.40	0.990 395 40	0.990 303 9	0.993 265 5	0.989 870 7
0.45	1.074 499 9	1.074 372	1.071 814 9	1.075 083 9
0.50	0.857 381 10	0.857 526 6	0.859 535	0.856 691 6
0.55	1.205 359 0	1.205 421	1.203 239 8	1.206 658 1
0.60	0.768 443 90	0.767 888 5	0.770 842 8	0.765 725 4
0.65	1.145 684 9	1.146 902 4	1.143 334 4	1.150 132 6
0.70	1.123 730 1	1.122 185 6	1.125 295 5	1.118 804 4
0.75	0.487 155 60	0.488 137 1	0.486 648 8	0.490 051
0.80	1.748 320 7	1.748 542 8	1.748 404 8	1.748 745
0.85	0.464 727 30	0.463 770 7	0.464 358 1	0.462 669 8
0.90	0.903 153 50	0.903 814 2	0.903 678 1	0.904 334 5
0.95	1.740 656 2	1.740 553 9	1.740 445	1.740 594
r	u_1^C	u_1^V	u_1^Z	
0.25	1.004 437 2	1.003 676	1.001 856 1	
0.30	1.006 511	1.004 387	1.004 480 9	
0.35	0.973 133 1	0.971 751	0.984 264 7	
0.40	0.989 953 1	0.995 357	0.989 222 6	
0.45	1.075 903 6	1.069 648	1.063 521 5	
0.50	0.855 174	0.861 564	0.875 303 4	
0.55	1.208 584 9	1.200 635	1.185 982 2	
0.60	0.763 908 4	0.775 048	0.782 729 3	
0.65	1.150 755 3	1.137 126	1.144 820 4	
0.70	1.120 815 6	1.132 144	1.104 336 3	
0.75	0.485 071 5	0.482 291	0.525 564 9	
0.80	1.754 340 5	1.747 759	1.705 207 3	
0.85	0.459 985 3	0.468 972	0.488 894 1	
0.90	0.903 639 4	0.899 133	0.914 518 8	
0.95	1.741 614	1.742 110	1.705 510 2	

(b) Comparison with the numerical simulation of the linearized momentum equation

A sample comparison between different velocity formulations is given in table 1 for parameters corresponding to a typical cold-flow experiment. It is reassuring to note the overall concurrence of various asymptotic techniques and the numerical solution of the linearized Navier–Stokes equation. This good agreement actually persists over a broad range of physical parameters. Using u_1^N as a benchmark, relative errors are determined and plotted in figure 3 for the first two oscillation modes and the same physical setting. Whereas discrepancies between most asymptotic solutions and u_1^N are almost too small to be discerned graphically, the error in u_1^Z exhibits large

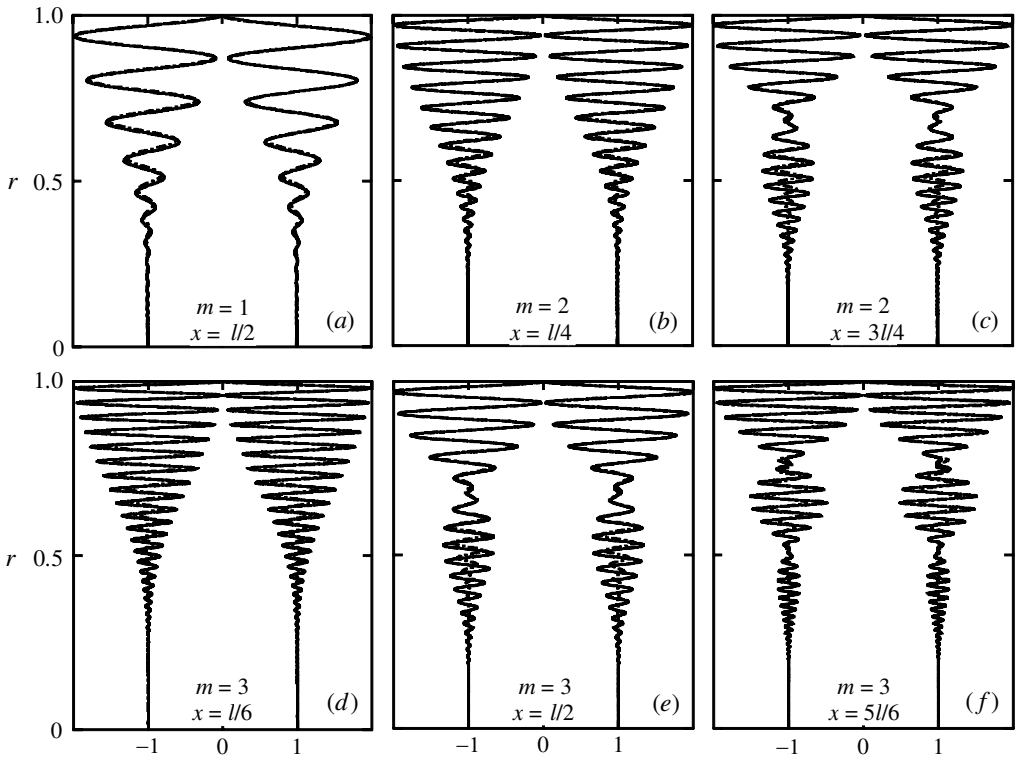


Figure 4. Comparison at two successive times between our asymptotic solution for u_1 (solid lines) and numeric simulations of the nonlinear Navier–Stokes equations (chains). For the first three oscillation modes, profiles are provided at axial positions corresponding to acoustic pressure nodes. Here $S = 50m$, $R = 4 \times 10^4$ and $\xi = m^2/16$. Discrepancies between numerics and asymptotics can be attributed, in part, to the finite mesh resolution of (a) 60×150 , (b), (c) 80×240 and (d)–(f) 90×360 (in the axial and radial directions) for $m = 1, 2$ and 3 .

random peaks that reflect non-uniformity. These random deviations become more pronounced at higher oscillation modes. This result can be attributed to the clear differences (shown in figure 2) between η^U and Zhao’s assumed function η^Z .

(c) Computational verification

The most striking result is, perhaps, the good agreement found when asymptotic predictions are compared with numerical simulations of the complete set of (nonlinear) Navier–Stokes equations. Inasmuch as small nonlinearities are not incorporated in the analytical derivations, deviations between asymptotics and numerical simulations turn out to be smaller than expected. A sample comparison is provided in figure 4 for the first three oscillation modes of a typical large injection case. While the axial locations are chosen to coincide with harmonic pressure nodes, results obtained are based on the fully implicit, finite-volume code developed by Roh *et al.* (1995). The small discrepancies between asymptotic and computational data are ascribed to the finite space and time discretization errors, and to small nonlinearities that elude the asymptotic model. Note, in particular, the presence of $j - 1$ rotational velocity nodes downstream of the j th internal velocity node in figure 4c, e, f. These

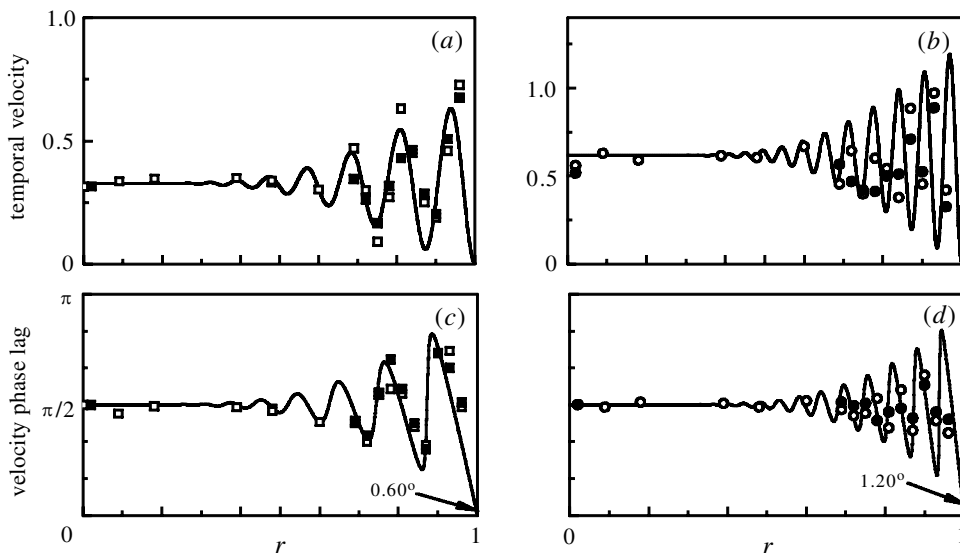


Figure 5. Comparison between our asymptotic solution for u_1 (solid lines) and experimental data obtained by Brown *et al.* (1986). For $m = 1$ and 2 , temporal velocity amplitudes are shown in (a) and (b) while their phase angles (with respect to pressure) are shown in (c) and (d). Similarity parameters correspond to $S = 51.3m$, $R = 4900$ and $x/l = 0.106$. Other parameters are $M = 0.0018$, $l = 34$, $\omega_m = (\pi/34)m$, and $\xi = 0.539m^2$. Hollow and dark symbols correspond to experimental data acquired with a pressure wave amplitude $\bar{\varepsilon}$ of 0.0005 and 0.0039 . Squares and circles are used to denote first and second oscillation modes. With reference to Brown *et al.* (1986), our symbols (\square), (\circ), (\blacksquare) and (\bullet) are for tables VI–IX.

premature nodes appear in the computational solution for $m > 1$ and concur with the forthcoming description. They do not appear in figure 4a, b, d, each of which is taken, for each oscillation mode m , at the axial location corresponding to the first internal pressure node upstream of the j th internal velocity mode.

(d) Experimental verification

In order to better understand the oscillatory flow character over transpiring surfaces, numerous velocity and pressure measurements have been gathered during cold-flow experiments conducted by Brown and co-workers (Brown *et al.* 1986; Dunlap *et al.* 1990). Their tests were carried out using a circular tube that allowed uniform, steady, sidewall injection of nitrogen gas. Their experimental set-up corresponded to $S = 51.3m$, $R = 4900$, $M = 0.0018$, $L = 1.727$ m, $a = 0.0508$ m, $c = 290$ m s $^{-1}$, $\nu = 5.43 \times 10^{-6}$ m 2 s $^{-1}$ and $\omega = 168\pi m$ rad s $^{-1}$. Using three-element hot-wire probes positioned in an upstream portion of the tube (where the flow is strongly laminar), experimental measurements were collected for the first two oscillation modes (84 and 168 Hz), and for two dimensionless pressure ratios (cf. tables VI–IX in Brown *et al.* (1986), pp. 120–123). While velocity amplitudes are shown in figure 5a, b for the first two oscillation modes, the velocity-to-pressure phase lags are compiled in figure 5c, d. Comparisons with asymptotic predictions show satisfactory agreement between theory and experiment. This agreement becomes more convincing when experimental acquisition and calibration errors are factored in. Note that, at the wall, the phase

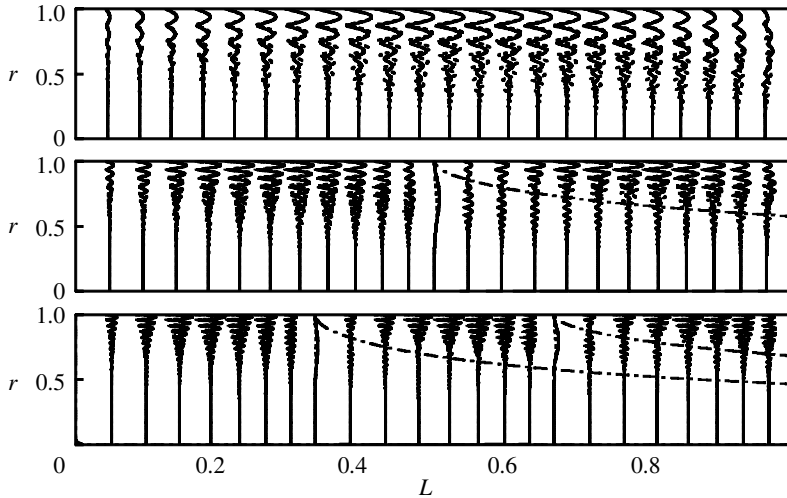


Figure 6. From top to bottom, the modulus of unsteady velocity is plotted at several axial locations and for the first three oscillation modes. Results are shown for geometrically similar tubes (solid lines) and channels (broken lines). Physical parameters are $R = 4 \times 10^4$, $\xi = m^2/16$ and $S = 50m$. A pattern correlation with classic acoustic mode shapes is apparent. Maximum rotational amplitudes occur near acoustic pressure nodes and diminish in the direction of velocity nodes. Rotational amplitudes are not symmetric with respect to pressure nodes as they increase downstream due to the mean-flow convection of unsteady vorticity. The presence of premature zero rotational amplitudes for $m = 2, 3$ are due to streaks of zero vorticity (chain lines) emanating from the j th internal velocity nodes located at $x/l = j/m$, $j < m$. The penetration of vorticity is more significant in a channel (broken lines).

lag can be calculated, following Majdalani (1999), to be $\pi/2 - \arctan(R/S)$. This result can be numerically verified $\forall F$.

(e) *Evolution of unsteady velocity and vorticity*

Unlike the vorticity-transport formulation, the generalized-scale solution is sufficiently compact to provide simple expressions for a number of flow features. Included are the depth of penetration, Richardson overshoot factor, phase lag and velocity modulus. The first three features have been covered, for large R , by Majdalani (1999). The arbitrary injection case can be similarly treated. The velocity modulus will be now examined because of its usefulness in describing the flow character across the tube's finite length.

For a typical test case, $|u_1|$ can be evaluated and is shown in figure 6 at several discrete locations. For the first three oscillation modes, patterns are clearly influenced by the inviscid pressure mode shapes. Rotational amplitudes are largest along the wall near harmonic pressure nodes where the pressure-driven velocity response is most intense. Pressure nodes may be identified by $x/l = (2j - 1)/2m$, $1 \leq j \leq m$, for the j th internal pressure node. The additional downstream intensification of rotational amplitudes is due to the axial convection of unsteady vorticity by the mean flow. Conversely, a weakening in vortical strength is noted during inward propagation. The vortical attenuation in the radial direction can be attributed to the compounding effects of viscous diffusion and the speed reduction in the convective motion.

Irrespective of the acoustic oscillation mode, one observes, near the wall, an overshoot in the unsteady velocity amplitude. Commonly referred to as the Richardson annular effect (cf. Rott 1964), this phenomenon is more intense near the wall where the large vortical response can favourably couple with the pressure-driven response.

At higher oscillation modes ($m > 1$), the presence of premature nodes of zero rotational amplitude is noted $j < m$ times downstream of the j th internal velocity node. These irrotational points are caused by the lines of zero vorticity that originate at the velocity nodes ($x/l = j/m$) and stretch across the solution domain. In fact, when $|u_1|$ is plotted at several axial locations, the rotational nodes are found to appear at the radial intersections with the zero vorticity streaklines.

Whereas acoustic velocity nodes correspond to zero vorticity points, the most appreciable vorticity sources appear at the pressure nodes. In fact, a close examination of (3.4) confirms that fresh vorticity is constantly supplied at the wall where the oscillatory pressure gradient in the axial direction is perpendicular to the radially incoming flow. Thus $\bar{\Omega}(x, 1)$ is highest at $x/l = (2j - 1)/2m$, where $\hat{p} = 0$ and \hat{u} exhibits the maximum amplitude given by (2.17). Since the total vorticity can be written as

$$\Omega = Mx(F'/r - F'')/r + \bar{\varepsilon}rS \sin[m\pi(x/l)F] \exp \zeta \cos(\omega_m t + \Phi), \quad (8.1)$$

it is clear that the maximum $\bar{\Omega}(x, 1)$ is of the order of $\bar{\varepsilon}S/M = \omega_m \bar{\varepsilon}/M^2$ in comparison with the steady vorticity. Recalling from (2.13) that $\bar{\varepsilon}/M^2 > 1$, it follows that unsteady vorticity can be more intense than the mean-flow vorticity. The role played by unsteady vorticity is hence very important and should not be discounted in this or similar low Mach number viscous models.

(f) Curvature effects

In order to illustrate the principal differences between axisymmetric and planar motions, results in figure 6 are shown for two geometrically similar ducts, namely, for a tube (solid lines) and a channel (broken lines) that exhibit circular and rectangular cross-sections. We find the inward penetration of vorticity to be more significant in a channel due to the absence of curvature. A curvature appears to inhibit the penetration depth of vorticity by reducing the flow cross-section normal to incoming streams. For the same reason, the unsteady velocity amplitude decays more rapidly in a tube.

With respect to mean vorticity generation and transport, two interesting features can be noted. The first regards vorticity amplitudes. By comparing the mean-flow velocity and vorticity in (2.2) to that in a channel (Majdalani & Roh 2000), one finds, for any position x ,

$$\frac{u_0(r=1)}{u_0(y=0)} = \begin{cases} \frac{8}{3}, & \Omega_0(r=0) \\ 2, & \Omega_0(y=1) \end{cases} = \begin{cases} \frac{8}{3}, & \text{small } R, \\ 4, & \text{large } R. \end{cases} \quad (8.2)$$

Hence, for large R , $\Omega_0 = \pi^2 x$ is four times larger near the wall in a tube than in a channel with $\Omega_0 = \frac{1}{4}\pi^2 x$. Reasons can be attributed to the larger axial velocity in the tube. The larger amplitudes are compounded by vortex augmentation caused by the radial compression of circular vortex rings. Such compression is not present in the less vortical channel having the same aspect ratio. As explained by Flandro

(1995*a*) and Majdalani *et al.* (2000), vorticity can lead to an important destabilizing term in solid rocket motor combustion that needs to be accounted for lest predictions fall short of actual measurements. From that perspective, an enhanced vortical field in a tube is likely to promote a less stable acoustic environment.

The second feature regards the transverse penetration of mean vorticity. Since vorticity is carried by the mean flow, its penetration depth is found to be more significant in a channel where a more gradual flow turning occurs. As flow turning requires energy to be transferred from the axial acoustic field to the radially incoming fluid, the energy exchange happens more rapidly near the walls of a tube. Despite the smaller local vorticity in the channel, the infinite radius of curvature allows vorticity rings to tap deeper into the core. Conversely, since a finite curvature inhibits the inward propagation of vorticity, a broader inviscid core is realized in a tube.

(*g*) *Comparison with Sexl's profile*

Since the mean flow is solely induced by the influx at the walls, suppressing injection drastically alters our model. As we approach the limiting process of zero injection, walls become impermeable and pressure loses its mean component. The question that could be raised is where should one stop? We find that, if V in our model is made comparable with the Stokes diffusion speed, $\sqrt{2\omega\nu}$, our results will mimic Sexl's exact solution for an oscillatory flow bounded by rigid walls. In that event, dynamic similarity parameters can be chosen such that $\xi = \lambda_S$, where $\lambda_S = a\sqrt{\omega/2\nu}$ is the Stokes number. Accordingly, we will have

$$R = 2^{1/6}a\sqrt{\omega/\nu} \quad \text{and} \quad V = \sqrt{2\omega\nu}/\sqrt[3]{2}.$$

The wall injection velocity will hence be slightly smaller than the diffusion speed. One may interpret this condition to be reflective of insignificant injection. The resulting field can be compared with the exact solution given by Sexl (1930) for an oscillating fluid inside an impermeable tube. The latter is derived for an infinitely long tube and exhibits first-mode oscillations that are independent of x . Due to our tube's finite length, we compare u_1 in figure 7 with the exact solution at $x/l = \frac{1}{2}$ and $m = 1$. Graphically, the comparison seems to indicate a favourable agreement between asymptotic and exact predictions. In particular, when injection is virtually absent, a reversal can be noted in the role played by viscosity. This phenomenon is consistent with Prandtl's classic theory foreseeing a deeper vortical presence with increased viscosity (figure 7*a*).

Overall, our approximate solution seems to embrace Sexl's solution when injection is reduced to the diffusion speed. Thus, although it is possible to approximate the one-dimensional oscillatory solution from ours, the converse is not true. Since $2^{1/6} \cong 1.12$, one may set the lower limit on the crossflow Reynolds number to be $R = a\sqrt{\omega/\nu} = 10$, so that $\varepsilon \leq 0.1$. This lower limit is prescribed, in part, by the desired precision in the ensuing perturbation analysis. At the lower end of the spectrum, properties must therefore satisfy $a\sqrt{\omega/\nu} > 10$ and $Va/\nu > 10$. The corresponding model remains applicable as long as

$$V > 10\nu/a \quad \text{and} \quad \omega > 10V/a. \quad (8.3)$$

These inequalities set the lower bounds for an open-ended range of physical parameter encompassing many realistic flows.

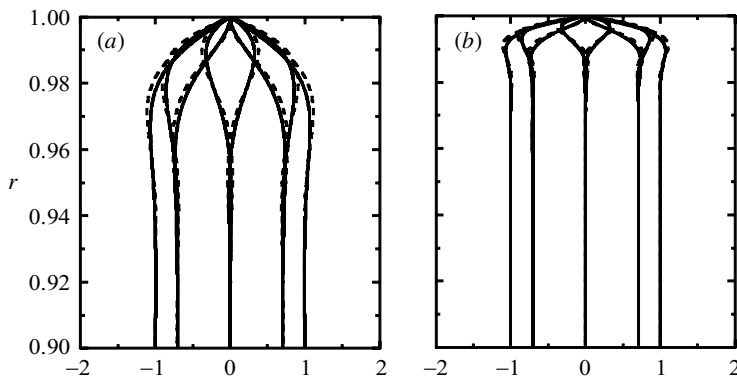


Figure 7. Velocity profiles of u_1 shown at eight successive time-intervals. Results are obtained from asymptotic predictions (broken lines) and the exact formula by Sexl (full lines). Parameters correspond to $\xi = \lambda_s$ for which convective and diffusive speeds are of the same order. We use $a\sqrt{\omega/\nu} = 100$ in (a) and $100\sqrt{10}$ in (b). In the absence of appreciable wall injection, the penetration of vorticity diminishes when viscosity is reduced, going from (a) to (b).

(h) Viscosity and the boundary layer

Observations made in the channel analogue regarding the role of viscosity are reconfirmed here for an arbitrary mean-flow function. For moderate-to-large injection speeds, the penetration depth is found to diminish with increasing viscosity. However, for sufficiently small injection, the depth of penetration decreases when viscosity is made smaller. In order to understand the seemingly paradoxical role played by viscosity, one needs to examine the details of the penetration depth, Δ^* . To begin, one needs to realize that Δ^* encompasses two adjacent regions: a highly vortical layer immediately above the wall followed by a highly viscous layer of $O(\sqrt{\nu/V})$ that is blown-off by the incoming stream.

For sufficiently small injection, the solution is a strongly damped wave whose viscous layer is formed in the close proximity of the wall. Moreover, it is much larger than the vortical layer pressed beneath it. The resulting depth of penetration becomes slightly larger than the Stokes layer of $O(\sqrt{\nu/\omega})$. Now when viscosity is increased, the viscous layer grows in size and the rate at which vorticity diffuses increases also. The enhanced diffusion rate causes the underlying vorticity layer to narrow in thickness. Since the vortical thickness is of order $V^3/(\omega^2\nu)$, it can be near zero for sufficiently small V ; as such, the net reduction in the vorticity sheet constitutes an insignificant contribution to the overall depth of penetration. The net growth in the viscous layer outweighs the net reduction in the thin vorticity layer to the point that a larger Δ^* is realized.

For appreciable injection reported in cold-flow studies, the highly viscous layer of $O(\sqrt{\nu/V})$ is now pushed to the central portion of the tube (Proudman 1960). It is much thinner than the vorticity layer of $O(a)$ (since $V^3/(\omega^2\nu) = a/\xi$ and $\xi \sim 1$). When viscosity is increased, the expansion of the thin viscous layer of $O(\nu^{1/2})$ becomes negligible in comparison with the contraction of $O(\nu^{-1})$ experienced by the vorticity layer. The ensuing Δ^* decreases when ν is made larger. In a sense, it is the relative sizes of vorticity and viscosity layers at different injection speeds that stand behind the dual roles played by viscosity.

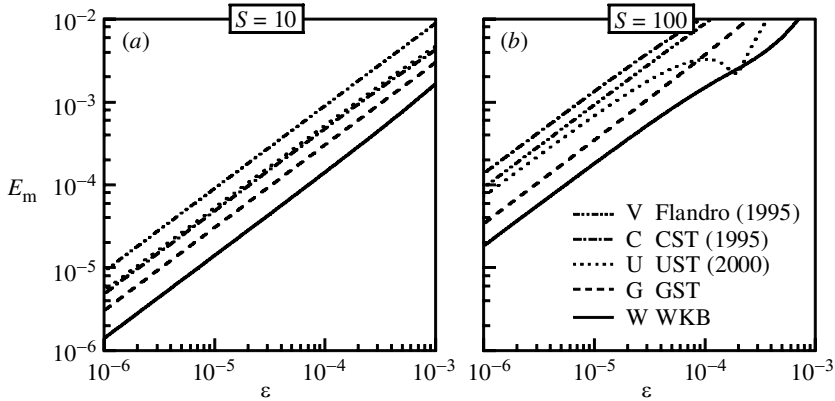


Figure 8. Comparison of maximum errors entailed in u_1^W , u_1^G , u_1^U , u_1^C and u_1^V for the large injection case. As $\varepsilon = R^{-1}$ is varied, the Strouhal number is held at (a) 10 and (b) 100. For every Strouhal number, the lowest curve that is indicative of the most accurate solution corresponds to u_1^W .

(i) Error verification

Using u_1^N as a benchmark, the asymptotic error associated with u_1^W , u_1^G , u_1^U , u_1^C and u_1^V can be evaluated. Following Bosley (1996), we define E_m to be the maximum absolute error between u_1^N and u_1 given asymptotically. Assuming a logarithmic variation of the form $E_m \propto \varepsilon^\alpha$, the slope α can be read from the log-log plot of E_m versus ε . This, of course, gives the order of the error. As we show in figure 8, $\alpha \rightarrow 1$ asymptotically in all cases. Pursuant to Bosley's arguments, the clear asymptotic behaviour indicates that all asymptotic solutions are correct, uniformly valid, and exhibit errors of $O(\varepsilon)$ over a wide range of parameters. The errors associated with u_1^W and u_1^G remain, however, the smallest. The improved accuracy of u_1^W is offset by the increased algebraic complexity in evaluating its first-order correction terms (see (4.14)). The simplicity, accuracy and ease of evaluating u_1^G make it our favourite solution.

9. Concluding remarks

The quest for exact or asymptotic solutions of the viscous flow equations in porous tubes has a long history. In this work, we have presented a comprehensive account of the forms of asymptotic approximations that can proceed from the linearized vorticity and momentum transport equations. In contrast to previous studies of this topic that have addressed specific physical settings, we have implemented a systematic investigation using a general form of the mean-flow field. Other authors have typically considered one level of injection in a given geometric setting. This work has demonstrated the possibility of presenting the final solution in a generic form that provides realizable expressions for any sufficiently differentiable mean-flow function F . The generalized formulations show how not only do we recover (e.g. u_1^U and u_1^V), confirm (u_1^C), or correct previously attempted solutions (u_1^Z), but also find some completely new asymptotic forms (u_1^G and u_1^W). These have been catalogued in their most simple forms in §§3–7. Any of them can be repeated for a more elaborate

setting that includes, for example, the effects of expanding or contracting walls, non-uniformly permeable boundaries, and suction instead of injection. They can also be used to study the onset of hydrodynamic instability in the tube. As such, they open new lines of further enquiry.

Our solutions are especially useful in correcting deficiencies in current predictive algorithms used to determine the system stability in solid rocket motors. By demonstrating that unsteady vorticity exceeds in magnitude its steady counterpart, we have established the importance of implementing the elements of vorticity, viscosity, and other flow interactions not incorporated previously. To avoid combustion instabilities late in the development cycle, corrective procedures that include vorticity effects, such as those developed here, must therefore be accommodated in the analysis of oscillatory flows in high energy propulsion systems and industrial burners.

From a physical standpoint, our formulations promote a complete flow characterization that displays interesting vorticity and velocity patterns. These patterns are strongly influenced by the acoustic pressure mode shapes. For example, we find the most significant sources of unsteady vorticity to be concentrated near pressure nodes (at $x/l = (2j - 1)/2m$, $1 \leq j \leq m$). By comparing tube and channel flows, our study brings into focus the effect of a tube's radius of curvature. In comparison with a channel, a tube is found to exhibit faster flow turning near the wall. It also induces magnifications in core velocities and vorticities by $(\frac{8}{3}, \frac{8}{3})$ and $(2, 4)$ for small and large R . While a smaller radius of curvature inhibits the inward penetration of mean and unsteady vorticity, it promotes larger vortical magnitudes.

It is reassuring that our mathematical models, which have been hypothetical in nature, could be corroborated by experimental and computational tests. It is also vital that our formulations could reproduce exact solutions (such as Sexl's) and confirm, correct, or recover previously reported approximations. In the case of the generalized-scale technique, the ensuing work encompasses a completely new and rigorous method of analysis. The underlying multiple-scale structure encountered here can be attributed to the co-evolution of radial convection and viscous diffusion of vorticity waves on separate radial dimensions. Similar interactions can be present in other convection–diffusion problems that have been, heretofore, impossible to solve.

References

- Barron, J., Majdalani, J. & Van Moorhem, W. K. 2000 A novel investigation of the oscillatory field over a transpiring surface. *J. Sound Vib.* **235**, 281–297.
- Beddini, R. A. 1986 Injection-induced flows in porous-walled ducts. *AIAA J.* **24**, 1766–1773.
- Bender, C. M. & Orszag, S. A. 1978 *Advanced mathematical methods for scientists and engineers*. McGraw-Hill.
- Berman, A. S. 1953 Laminar flow in channels with porous walls. *J. Appl. Phys.* **24**, 1232–1235.
- Bosley, D. L. 1996 A technique for the numerical verification of asymptotic expansions. *SIAM Rev.* **38**, 128–135.
- Brady, J. F. 1984 Flow development in a porous channel or tube. *Phys. Fluids* **27**, 1061–1067.
- Brady, J. F. & Acrivos, A. 1981 Steady flow in a channel or tube with an accelerating surface velocity. An exact solution to the Navier–Stokes equations with reverse flow. *J. Fluid Mech.* **112**, 127–150.
- Brown, R. S., Blackner, A. M., Willoughby, P. G. & Dunlap, R. 1986 Coupling between velocity oscillations and solid propellant combustion. Final Tech. Rep. F49620-81-C-0027. Bolling Air Force Base.

- Casalis, G., Avalon, G. & Pineau, J.-P. 1998 Spatial instability of planar channel flow with fluid injection through porous walls. *Phys. Fluids* **10**, 2558–2568.
- Culick, F. E. C. 1966 Rotational axisymmetric mean flow and damping of acoustic waves in a solid propellant rocket. *AIAA J.* **4**, 1462–1464.
- Dunlap, R., Blackner, A. M., Waugh, R. C., Brown, R. S. & Willoughby, P. G. 1990 Internal flow field studies in a simulated cylindrical port rocket chamber. *J. Propul. Power* **6**, 690–704.
- Durlofsky, L. & Brady, J. F. 1984 The spatial stability of a class of similarity solutions. *Phys. Fluids* **27**, 1068–1076.
- Flandro, G. A. 1974 Solid propellant acoustic admittance corrections. *J. Sound Vib.* **36**, 297–312.
- Flandro, G. A. 1989 Effects of vorticity transport on axial acoustic waves in a solid propellant rocket chamber. In *Combustion instabilities driven by thermo-chemical acoustic sources*, NCA, vol. 4, pp. 53–61. New York: American Society of Mechanical Engineers.
- Flandro, G. A. 1995a Effects of vorticity on rocket combustion stability. *J. Propul. Power* **11**, 607–625.
- Flandro, G. A. 1995b On flow turning. AIAA Paper 95-2530.
- Gol'dshtik, M. A. & Ersh, N. M. 1989 Stability of pipe flow with blowing. *Fluid Dynam.* **24**, 51–59.
- Goto, M. & Uchida, S. 1990 Unsteady flows in a semi-infinite expanding pipe with injection through wall. *Trans. Jpn Soc. Aeronaut. Space Sci.* **33**, 14–27.
- Griffond, J. & Casalis, G. 2001 On the nonparallel stability of the injection induced two-dimensional Taylor flow. *Phys. Fluids* **13**, 1635–1644.
- Lu, C. 1994 On the existence of multiple solutions of a boundary value problem arising from laminar flow through a porous pipe. *Can. Appl. Math. Q.* **2**, 361–393.
- Ma, Y., Van Moorhem, W. K. & Shorthill, R. W. 1990 Innovative method of investigating the role of turbulence in the velocity coupling phenomenon. *ASME J. Vib. Acoust.* **112**, 550–555.
- Ma, Y., Van Moorhem, W. K. & Shorthill, R. W. 1991 Experimental investigation of velocity coupling in combustion instability. *J. Propul. Power* **7**, 692–699.
- Majdalani, J. 1998 A hybrid multiple scale procedure for boundary layers involving several dissimilar scales. *Z. Angew. Math. Phys.* **49**, 849–868.
- Majdalani, J. 1999 The boundary layer structure in cylindrical rocket motors. *AIAA J.* **37**, 505–508.
- Majdalani, J. & Roh, T. S. 2000 The oscillatory channel flow with large wall injection. *Proc. R. Soc. Lond. A* **456**, 1625–1657.
- Majdalani, J. & Van Moorhem, W. K. 1995 The unsteady boundary layer in solid rocket motors. AIAA Paper 95-2731.
- Majdalani, J. & Van Moorhem, W. K. 1997 A multiple-scales solution to the acoustic boundary layer in solid rocket motors. *J. Propul. Power* **13**, 186–193.
- Majdalani, J. & Van Moorhem, W. K. 1998 Improved time-dependent flowfield solution for solid rocket motors. *AIAA J.* **36**, 241–248.
- Majdalani, J., Flandro, G. A. & Roh, T. S. 2000 Convergence of two flowfield models predicting a destabilizing agent in rocket combustion. *J. Propul. Power* **16**, 492–497.
- Munson, A. G. 1964 The vortical layer on an inclined cone. *J. Fluid Mech.* **20**, 625–643.
- Olson, R. M. & Eckert, E. R. G. 1966 Experimental studies of turbulent flow in a porous circular tube with uniform fluid injection through the tube wall. *Trans. ASME J. Appl. Mech.* **33**, 7–17.
- Proudman, I. 1960 An example of steady laminar flow at large Reynolds number. *J. Fluid Mech.* **9**, 593–612.
- Roh, T. S., Tseng, I. S. & Yang, V. 1995 Effects of acoustic oscillations on flame dynamics of homogeneous propellants in rocket motors. *J. Propul. Power* **11**, 640–650.

- Rott, N. 1964 Theory of time-dependent laminar flows. In *High speed aerodynamics and jet propulsion—theory of laminar flows* (ed. F. K. Moore), vol. IV, pp. 395–438. Princeton University Press.
- Sexl, T. 1930 Über den von E. G. Richardson entdeckten ‘Annulareffekt’. *Z. Phys.* **61**, 349–362.
- Skalak, F. M. & Wang, C.-Y. 1978 On the nonunique solutions of laminar flow through a porous tube or channel. *SIAM J. Appl. Math.* **34**, 535–544.
- Sviridenkov, A. A. & Yagodkin, V. I. 1976 Flow in the initial sections of channels with permeable walls. *Fluid Dynam.* **11**, 689–693.
- Taylor, G. I. 1956 Fluid flow in regions bounded by porous surfaces. *Proc. R. Soc. Lond. A* **234**, 456–475.
- Terrill, R. M. 1973 On some exponentially small terms arising in flow through a porous pipe. *Q. J. Mech. Appl. Math.* **26**, 347–354.
- Terrill, R. M. 1983 Laminar flow through a porous tube. *ASME J. Fluids Engng* **105**, 303–307.
- Terrill, R. M. & Thomas, P. W. 1969 On laminar flow through a uniformly porous pipe. *Appl. Scient. Res.* **21**, 37–67.
- Van Dyke, M. 1975 *Perturbation methods in fluid mechanics*. Stanford, CA: The Parabolic Press.
- Wageman, W. E. & Guevara, F. A. 1960 Fluid flow through a porous channel. *Phys. Fluids* **3**, 878–881.
- Weissberg, H. L. 1959 Laminar flow in the entrance region of a porous pipe. *Phys. Fluids* **2**, 510–516.
- Yuan, S. W. & Brogren, E. W. 1961 Turbulent flow in a circular pipe with porous walls. *Phys. Fluids* **4**, 368–372.
- Yuan, S. W. & Finkelstein, A. B. 1956 Laminar pipe flow with injection and suction through a porous wall. *Trans. ASME J. Appl. Mech.* **78**, 719–724.
- Zhao, Q., Staab, P. L., Kassoy, D. R. & Kirkköprü, K. 2000 Acoustically generated vorticity in an internal flow. *J. Fluid Mech.* **413**, 247–285.